Nuclear incoherent photoproduction of π^0 and η from 4 to 12 GeV

T. E. Rodrigues,[1] J. D. T. Arruda-Neto,[1,2] J. Mesa,[3] C. Garcia,[4] K. Shtejer,[1,4] D. Dale,[5] I. Nakagawa,[6] and P. L. Cole[5]

[1]*Physics Institute, University of São Paulo, P.O. Box 66318, CEP 05315-970, São Paulo, Brazil*

[2]*FESP, São Paulo Engineering College, São Paulo, Brazil*

[3]*Department of Physics and Biophysics, UNESP, Botucatu, Brazil*

[4]*Center of Applied Studies for Nuclear Developments (CEADEN), Havana, Cuba*

[5]*Department of Physics, Idaho State University, Pocatello, Idaho 83209, USA*

[6]*RIKEN 2-1 Hirosawa, Wako, Saitama 351-0198, Japan*

(Received 9 April 2010; published 20 August 2010)

The mechanism of incoherent π^0 and η photoproduction from complex nuclei is investigated from 4 to 12 GeV with an extended version of the multicollisional Monte Carlo (MCMC) intranuclear cascade model. The calculations take into account the elementary photoproduction amplitudes via a Regge model and the nuclear effects of photon shadowing, Pauli blocking, and meson-nucleus final-state interactions. The results for π^0 photoproduction reproduced for the first time the magnitude and energy dependence of the measured rations $\sigma_{\gamma A}/\sigma_{\gamma N}$ for several nuclei (Be, C, Al, Cu, Ag, and Pb) from a Cornell experiment. The results for η photoproduction fitted the inelastic background in Cornell's yields remarkably well, which is clearly not isotropic as previously considered in Cornell's analysis. With this constraint for the background, the $\eta \to \gamma\gamma$ decay width was extracted using the Primakoff method, combining Be and Cu data [$\Gamma_{\eta\to\gamma\gamma} = 0.476(62)$ keV] and using Be data only [$\Gamma_{\eta\to\gamma\gamma} = 0.512(90)$ keV]; where the errors are only statistical. These results are in sharp contrast ($\sim$50–60%) with the value reported by the Cornell group [$\Gamma_{\eta\to\gamma\gamma} = 0.324(46)$ keV] and in line with the Particle Data Group average of 0.510(26) keV.

DOI: 10.1103/PhysRevC.82.024608 PACS number(s): 25.20.Lj, 24.10.Lx, 12.40.Nn, 12.40.Vv

I. INTRODUCTION

The possibility of extracting the radiative decay width of pseudoscalar mesons ($P \equiv \pi^0$, η, and η') into two photons ($\Gamma_{P\to\gamma\gamma}$) using photoproduction data from complex nuclei was first proposed by H. Primakoff in 1951 [1]. The method allows the determination of the decay width by the disentanglement of the electromagnetic component of the meson angular distributions at forward angles. The procedure requires a detailed understanding of the relevant photoproduction channels, since the mesons can also be produced in the strong field of complex nuclei either coherently or incoherently. The nuclear coherent photoproduction is satisfactorily described under the integral formalism developed by Glauber [2] and will not be discussed in this work, which is dedicated to the incoherent part only.

Using the impulse approximation (IA) and assuming closure, the nuclear incoherent photoproduction cross section can be expressed in terms of single nucleon amplitudes, as elegantly presented in Ref. [3]. The photoproduction mechanism is caracterized by an excited nucleus in the final state with or without the nuclear breakup. Such complicated mechanism depends very critically on the initial photoproduction channel, as well as on the nuclear effects. The calculation of the nuclear amplitude for incoherent photoproduction can also be performed under the context of the Glauber model [2]. The main advantage of the Glauber approach is that the integral formalism allows the derivation of analytical and general expressions for the incoherent photoproduction cross section, as recently proposed by S. Gevorkyan *et al.* [4]. However, as discussed further in this article, the Glauber approach has some limitations to account for short-range correlations in secondary meson-nucleon scatterings, local density fluctuations, and energy losses due to the nuclear excitation and meson-nucleus final-state interactions (FSI). Moreover, the Glauber formalism has some restrictions for the implementation of nuclear structure aspects of light nuclei, such as the momentum distribution (MD) of the bound nucleons. Consequently, a completely new approach based on a sophisticated multicollisional Monte Carlo (MCMC) intranuclear cascade model is proposed here to improve the description of incoherent photoproduction. As will be presented later, the cascade model couples for the first time an accurate description of the initial photon-nucleon interaction based on a Regge model with important nuclear effects relevant in high-energy photon-nucleus interactions. The comparison between our results for π^0 photoproduction with the recent results from Ref. [4] will be presented in Sec. IV.

Except the Glauber model, the calculations developed so far for incoherent π^0 and η photoproduction from complex nuclei have been usually concentrated within the nucleon resonances. For instance, the cross section for incoherent η photoproduction up to $\sim$1 GeV is dominated by the $S_{11}(1535)$ resonance excitation due to its large branching ratio decay into the $N\eta$ channel. Similarly, for the case of incoherent π^0 photoproduction most of the theoretical predictions have been provided up to $\sim$1 GeV, following the general tendency of recent experiments performed at the Mainz Microtron Facility [5,6]. The meson-nucleus FSI have been taken into account using optical potentials [7], classical propagation between meson-nucleon collisions [8], the quantum molecular dynamics (QMD) model of Ref. [9], or the Boltzmann-Uehling-Uhlenbeck (BUU) transport model [10]. All of these theoretical contributions have specific features not discussed in this article and represent important developments for the

investigation of meson photoproduction within the nucleon resonances. On the other hand, the calculations include only a limited number of photoproduction channels and are not supposed to describe incoherent photoproduction at forward angles and higher energies (4 to 12 GeV), the aim of this work.

The radiative decay width of the neutral pion ($\Gamma_{\pi^0\to\gamma\gamma}$) has been subject to intense experimental and theoretical efforts since the advent of the PrimEx Collaboration at the Jefferson Laboratory [11]. Recent calculations based on chiral perturbation theory (ChPT) [12–14] showed a typical 4% enhancement in the decay width compared with the axial anomaly prediction [15]. Such increase was most likely dominated by the isospin-breaking–induced mixing of the pure SU(3) states η and η'. Another correction of a much smaller magnitude to the leading order $\pi^0 \to \gamma\gamma$ amplitude was attributed to excited mesonic states using QCD sum rules [16]. The connection between the π^0 and η radiative decay widths is evident since the latter is a necessary input to obtain the former beyond the chiral anomaly prediction [12–14,16]. Consequently, more accurate measurements of the $\eta \to \gamma\gamma$ decay width are also strongly encouraged with the forthcoming 12-GeV upgrade at the Jefferson Laboratory. Obviously, this renewed interest in the Primakoff method also requires a detailed understanding—proposed in the present work—of the incoherent background both for π^0 and η photoproduction up to 12 GeV.

The $\eta \to \gamma\gamma$ decay width has been measured in collider experiments [17–22] and also using the Primakoff method at Cornell [23]. There is also another Primakoff-type experiment [24], but the uncertainty from the separation of the Coulomb and nuclear contributions was probably underestimated. The collider measurements are in overall agreement, while the Primakoff-type measurement from Cornell is significantly lower [0.324(46) keV] and was recently excluded from the Particle Data Group (PDG) world average of 0.510(26) keV [25]. This huge discrepancy between Cornell's and collider measurements provided strong evidence of an inadequate analysis of the inelastic background embedded in the η photoproduction yields from Cornell.

As we have shown in a recent Letter [26], the inelastic background in Cornell's data for η photoproduction from Be and Cu at $E_b = 9$ GeV could be safetly attributed to the nuclear incoherent (NI) cross sections obtained via the MCMC model. On the other hand, such contribution is largely Pauli suppressed at forward angles and cannot be approximated by an isotropic distribution; a procedure adopted in Cornell's analysis. The decay width extracted by fitting Cornell's data with the MCMC NI background is 0.476(62) keV, where the quoted error is only statistical. Therefore, our previous work [26] brought the $\eta \to \gamma\gamma$ decay width from Cornell in line with collider measurements, despite the fact that we have neglected the experimental systematic errors. It is worth mentioning, however, that our reanalysis is not supposed to supersede Cornell's measurement; a next-generation high-precision experiment is recommended for this purpose. The goal of our calculation was the delineation of the incoherent background, a necessary condition to support the Primakoff method in future measurements of the $\eta \to \gamma\gamma$ decay width. The details of our previous analysis [26] will be presented in Sec. IV.

The MCMC model consists of a relativistic and time-dependent Monte Carlo algorithm that describes the dynamics of an excited nuclear ensemble in terms of successive and time-ordered binary collisions. The photoproduction mechanism is described via a two-step process: (i) meson photoproduction from a single nucleon (IA) and (ii) meson-nucleus FSI via a cascade approach. An earlier version of the MCMC model [27] has been successfully applied for the interpretation of recent data of incoherent π^0 photoproduction from MAMI [5]. Another version [28] also investigated coherent π^0 photoproduction (electromagnetic/nuclear) including the nuclear recoil.

The basic features and improvements of the MCMC model discussed in this article are the following: (i) the use of time-dependent multicollisional relativistic kinematics, (ii) the inclusion of the meson photoproduction mechanism (π^0 and η) from 4.0 to 12.0 GeV via a Regge model (ρ and ω exchange included), (iii) the incorporation of accurate momentum distributions for light nuclei taken from nucleon knock-out reactions, (iv) a rigorous nonstochastic Pauli blocking both for the photoproduction and binary meson-nucleon scatterings, (v) the implementation of photon shadowing effects using a vector-meson dominance (VMD) model with vector-meson formation time constraint, (vi) a consistent analysis of the meson-nucleus FSI via a multiple scattering framework, and (vii) the inclusion of realistic (diffractive) angular distributions for the $PN \to PN$ elastic scattering.

The article is organized as follows. In Sec. II we present a Regge model to describe the elementary photoproduction amplitude for π^0 and η photoproduction from the nucleon. Section III is dedicated to the nuclear incoherent photoproduction, where we delineate the basic features of the MCMC model to account for the nuclear effects. In Sec. IV we show the results of the MCMC model in comparison with the available data. The calculations for incoherent π^0 photoproduction are successfully applied for the interpretation of the magnitude and energy dependence of the measured ratio $\sigma_{\gamma A}/\sigma_{\gamma N}$ taken for several nuclei (Be, C, Al, Cu, Ag, and Pb) at Cornell [29]. In this section we also present a detailed explanation for the incoherent background of η mesons in another Cornell experiment [23], extracting the $\eta \to \gamma\gamma$ decay width via the Primakoff method. The conclusions and final remarks are presented in Sec. V.

II. PSEUDOSCALAR MESON PHOTOPRODUCTION FROM THE NUCLEON: THE CASCADE TRIGGER

The elementary photoproduction of a pseudoscalar meson P from the nucleon is represented by the following process:

$$\gamma(k) + N(p_1) \to P(p) + N(p_2), \tag{1}$$

where k, p_1, p, and p_2 represent the four-momentum of the incoming photon, struck nucleon, produced meson, and outgoing nucleon, respectively.

The differential cross section for meson photoproduction from the nucleon at small angles in the center of mass of the

s channel can be written as [27,30]:

$$\frac{d\sigma_n}{d\Omega} \cong |f_1 - f_2|^2 + \frac{\theta_*^2}{2}[|f_3 + f_4|^2 + 2\,\mathrm{Re}(f_1^* f_2 + f_1^* f_4 + f_2^* f_3)], \quad (2)$$

where the f_i's are the Pauli-type amplitudes [31] and θ_* is the polar angle of the photoproduced meson in the center of mass of the s channel. The f_i's amplitudes are functions of the invariant amplitudes $A_i = A_i(s,t)$, with $s = (k + p_1)^2$ and $t = (k - p)^2$ the usual Mandelstam variables. The relationship between the Pauli-type amplitudes f_i's and the analytical amplitudes A_i's is given by Refs. [30,31], where we have assumed that the initial and final nucleon energies are the same.

By decomposing the invariant amplitudes A_i in terms of regularized and parity-conserving t-channel helicity amplitudes F_i, we obtain [32,33]:

$$A_1 = -\frac{tF_1 + 2m_N F_3}{t - 4m_N^2} \quad (3)$$

$$A_2 = \frac{F_1}{t - 4m_N^2} + \frac{1}{t}\left(F_2 + \frac{2m_N F_3}{t - 4m_N^2}\right) \quad (4)$$

$$A_3 = -F_4 \quad (5)$$

$$A_4 = -\frac{2m_N F_1 + F_3}{t - 4m_N^2}, \quad (6)$$

where m_N is the nucleon mass.

The amplitudes F_2 (unnatural parity exchange) and F_3 (natural parity exchange) receive contributions from different trajectories, while the amplitudes A_i are known to be free of kinematical singularities [30]. Since Eq. (4) has a pole at $t = 0$, one is forced to postulate the "conspiracy relation" at zero-momentum transfer suitable for π^0 and η photoproduction [33]:

$$F_3(s, t = 0) = 2m_N F_2(s, t = 0). \quad (7)$$

So, using Eqs. (3)–(7) and writing Eq. (2) in terms of the F_i's, we have [32]:

$$\frac{d\sigma_n}{d\Omega} = \frac{p_*^2}{\pi}\frac{d\sigma_n}{dt} = \frac{p_*^2}{32\pi^2}\left\{\frac{F_3^2}{2m_N^2} - \left[t + \left(\frac{\mu^2}{2k_*}\right)^2\right] \times \left[\frac{F_1^2}{4m_N^2} + \frac{F_3^2}{16m_N^4} + \frac{F_1 F_3}{2m_N}\frac{1}{p_*\sqrt{s}}\right]\right\}, \quad (8)$$

where μ is the meson mass. Equation (8) is the same as Eq. (5) from Ref. [26] imposing the conspiracy relation $F_3 = 2m_N F_2$. The helicity-flip unnatural parity exchange amplitude F_4 is neglected in Ref. [26] and also in the present analysis since it goes with t and does not contribute significantly at forward angles.

The remaining helicity amplitudes F_1 and F_3 are then calculated using a Regge model that includes ω and ρ exchange (VMD model) and the Reggeon cuts, as suggested in Ref. [34]. In contrast with our previous work for η photoproduction [26], the b_1 meson exchange was neglected in the present analysis since we found that its contribution is very small and cannot be unambiguously separated from the other terms with the limited amount of forward-angle data available. Therefore, we adopted a more concise formula [Eq. (8)] that simultaneously fits both data sets of π^0 and η photoproduction within the desired energy range.

The natural-parity exchange amplitudes F_1 and F_3 are then calculated in terms of pole and cut contributions [34]:

$$F_1 \to F_1^{\rho} + F_1^{\omega} + F_1^{\mathrm{cut}} \quad (9)$$

$$F_3 \to F_3^{\rho} + F_3^{\omega} + F_3^{\mathrm{cut}} \quad (10)$$

where

$$F_1^{\rho,\omega}(s,t) = \frac{\sqrt{2}}{m_N}\gamma_1^{\rho,\omega}\frac{1 - e^{-i\pi\alpha(t)}}{\sin[\pi\alpha(t)]}\alpha(t) \times [1 + \alpha(t)]\,[2 + \alpha(t)]\left(\frac{s}{s_0}\right)^{\alpha(t)-1}, \quad (11)$$

$$F_1^{\mathrm{cut}}(s,t) = \frac{\sqrt{2}}{m_N}\gamma_1^{\mathrm{cut}}\frac{1 - e^{-i\pi\alpha(0)}}{\sin[\pi\alpha(0)]}\left(\frac{s}{s_0}\right)^{\alpha(0)-1}\frac{e^{at}}{\ln\left(\frac{s}{s_0}\right)}, \quad (12)$$

$$F_3^{\rho,\omega}(s,t) = \frac{2\sqrt{2}}{m_N}t\gamma_3^{\rho,\omega}\frac{1 - e^{-i\pi\alpha(t)}}{\sin[\pi\alpha(t)]}\alpha(t) \times [1 + \alpha(t)]\,[2 + \alpha(t)]\left(\frac{s}{s_0}\right)^{\alpha(t)-1}, \quad (13)$$

$$F_3^{\mathrm{cut}}(s,t) = 2\sqrt{2}\gamma_3^{\mathrm{cut}}\frac{1 - e^{-i\pi\alpha(0)}}{\sin[\pi\alpha(0)]}\left(\frac{s}{s_0}\right)^{\alpha(0)-1}\frac{e^{at}}{\ln\left(\frac{s}{s_0}\right)}. \quad (14)$$

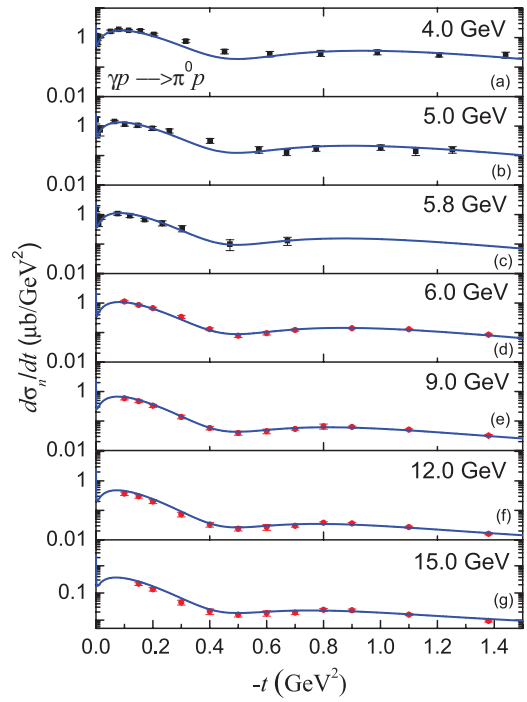

FIG. 1. (Color online) Differential cross section for π^0 photoproduction on the proton. The blue lines represent our Regge model with the Coulomb amplitude constructively interfering with F_1. The data points are from DESY [34] (squares) and SLAC [36] (triangles). The first data points from DESY [34] taken at $\theta_*^{\pi^0} = 0$ are omitted in our fitting due to the effects of angular resolution neglected in our analysis.

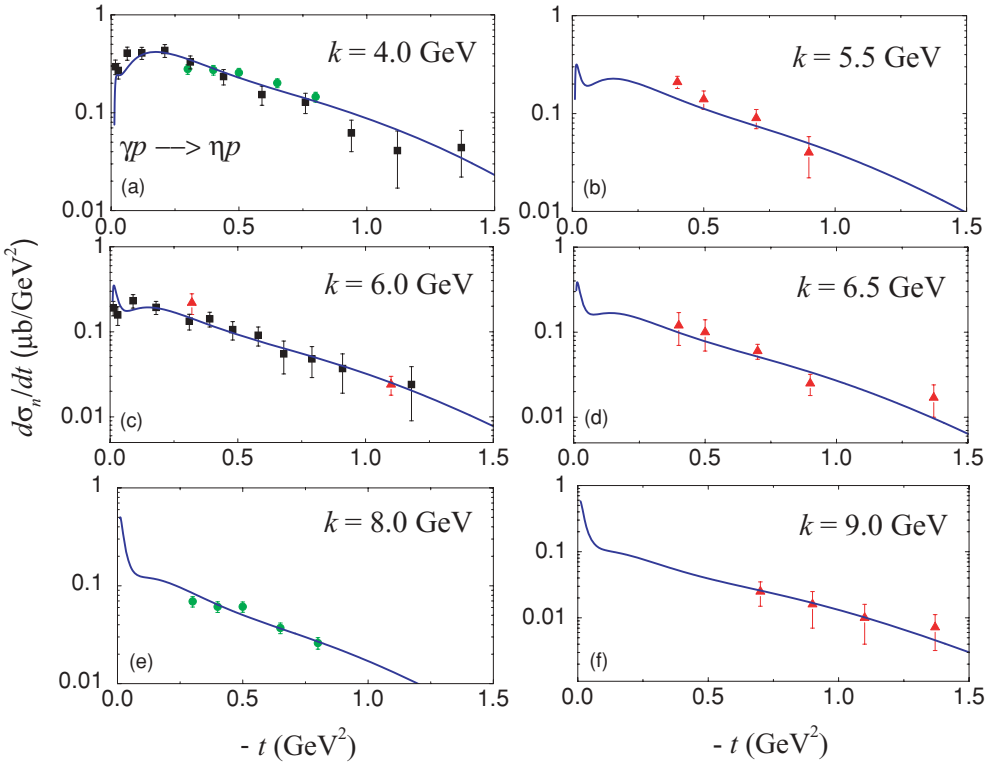

FIG. 2. (Color online) Differential cross section for η photoproduction on the proton. The blue lines represent our Regge model with the Coulomb amplitude destructively interfering with F_1. The data points are from DESY [35] (squares), SLAC [37] (triangles), and Cornell [38] (circles).

The Regge trajectories (same for ρ and ω exchange) were taken as $\alpha(t) = 0.45 + 0.9t$ for π^0 photoproduction and $\alpha(t) = 0.39 + 1.0t$ for η photoproduction, with $s_0 = 1$ GeV^2.

The parameters $\gamma_1 = \gamma_1^\rho + \gamma_1^\omega$, $\gamma_3 = \gamma_3^\rho + \gamma_3^\omega$, $\gamma_1^{\rm cut}$, $\gamma_3^{\rm cut}$, and a are obtained by fitting the available data of π^0 and η photoproduction from the proton also including the Coulomb amplitude:

$$F^C(s,t) = -\frac{2m_N}{t} 0.0543 \sqrt{\Gamma_{P\to\gamma\gamma}} \frac{1}{\left(1 + \frac{q_t^2}{0.71}\right)^2},$$

where we have used the PDG [25] recommended values $\Gamma_{\pi^0\to\gamma\gamma} = 7.7$ eV and $\Gamma_{\eta\to\gamma\gamma} = 0.510$ keV, with q_t representing the transverse-momentum transfer. The results of the fits for π^0 and η photoproduction are presented in Figs. 1 and 2, respectively; where a nice agreement between the Regge model and the data is achieved. The forward-angle data included in our analysis are from DESY [34,35], SLAC [36,37], and Cornell [38]. The constructive interference between the strong and Coulomb amplitudes is highly favorable for π^0 photoproduction ($F_1 \to F_1 + F^C$), while for η photoproduction the situation is opposite ($F_1 \to F_1 - F^C$). Table I summarizes the results of the fitted parameters of the Regge model. The inclusion of the Coulomb term is crucial to fit the data at forward angles, as shown in Fig. 3, where we present the prediction of the Regge model with and without the Coulomb term for π^0 photoproduction at 5.8 GeV.

The inclusion of the b_1 trajectory and the other terms of Eq. (5) of Ref. [26] does not change the overall fitting obtained for η photoproduction, since the contribution of Reggeon cuts tends to compensate the absence of b_1 exchange. In our previous work [26], we obtained χ^2/DOF ~ 1.4 in comparison with the present result of approximately 1.43. A similar situation is also found for π^0 photoproduction, where we got a reasonably good fitting neglecting b_1 exchange (χ^2/DOF $\sim$ 1.57). Such interesting scenario shows that the Regge model herein presented is not unique and other parametrizations

TABLE I. Fitted parameters of the Regge model for π^0 and η photoproduction from the proton. Details in the text.

Meson	$\gamma_1(\sqrt{\mu b})$	$\gamma_3(\sqrt{\mu b})$	$\gamma_1^{\rm cut}(\sqrt{\mu b})$	$\gamma_3^{\rm cut}(\frac{\sqrt{\mu b}}{\rm GeV})$	a(GeV^{-2})	$\frac{\chi^2}{\rm DOF}$
π^0	127.2(15)	61.6(17)	33.88(65)	10.23(23)	0.668(12)	$\frac{111.2}{73}$
η	44.3(51)	27.2(39)	155.4(24)	8.9(11)	2.059(26)	$\frac{61.6}{43}$

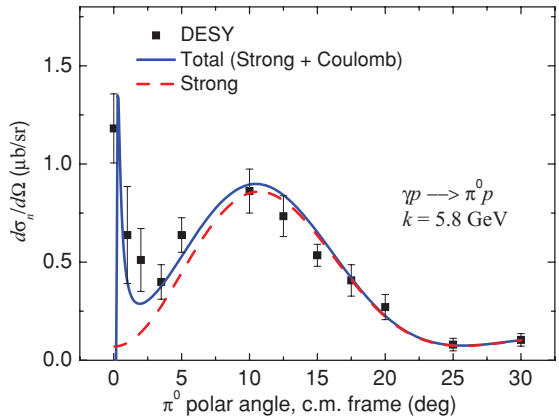

FIG. 3. (Color online) Differential cross section for π^0 photoproduction on the proton. The solid blue line represents our Regge model with the Coulomb amplitude constructively interfering with F_1 and the dashed red line includes only the strong part. The data points are from DESY [34] (squares), where the first point at $\theta^{\pi^0}_* = 0^0$ is omitted in the fitting due to the effects of angular resolution neglected in our analysis.

would certainly provide plausible interpretations of the proton data both for π^0 and η photoproduction. A detailed analysis of the elementary amplitude for π^0 photoproduction from 3 to 18 GeV was recently published by Sibirtsev *et al.* [39]. This work used a Regge model with pole and cut amplitudes for ω, ρ, and b_1 exchanges and reproduced quite satisfactorely a larger data set of the differential cross sections and single and double polarization observables for π^0 photoproduction. Nevertheless, as presented in Table 3 of Ref. [39], the model uses 17 free parameters in order to achieve a global fitting to the data. Furthermore, the F_1 amplitude was obtained without the Coulomb term and omitting the interference region $|t| < 0.04$ GeV^2 of the differential cross section; a crucial region included in our analysis. Such restriction of the analysis from Ref. [39] is strong evidence of the poor experimental scenario of the differential cross sections of π^0 photoproduction at extreme forward angles, making it difficult to establish one unambiguous Regge model for the interpretation of the data. This scenario is even more critical for η photoproduction, where data at extreme forward angles is provided only up to 6 GeV (Fig. 2). A recent Regge model calculation [40] has shown the importance of future forward-angle η photoproduction measurements from the proton. This analysis propitiated the extraction of the $\eta \to \gamma\gamma$ decay width by fitting the proton data, where the authors found values two to three σ larger than the PDG average [0.86(11) and 0.70(90) keV]. The fits, though quite interesting, assume that the decay width is uncorrelated with the other parameters used to fit the hadronic part. In our understanding, however, the decay width obtained by a fitting procedure to the angular distributions (Primakoff approach) should be correlated with the hadronic parameters and the interference phase angle. It would be interesting to verify a simultaneous (correlated) fitting with the model of Ref. [40]. The contribution of Regge cuts (absorptive part) on the hadronic amplitude is still unclear. Obviously the interpretation of the beam and target asymmetries done in Ref. [40] represents a significant improvement for the disentanglement of the natural and unnatural parity exchange amplitudes. However, at extreme forward angles, the conspiracy relation takes place $F_3 \sim 2m_N F_2$ and the beam and target asymmetries are close to 1 and zero, respectively. In fact, the effects of polarization are relevant only for $|t| \gtrsim 0.5$ GeV^2 (see Fig. 3 from Ref. [40]), where the incoherent cross section is expected to be quite small. So, the sophisticated calculation of Ref. [40] is very relevant with the advent of more precise forward-angle data. On the other hand, the determination of the decay width with high accuracy using only the proton target, though representing a much more clean measurement, seems unfeasible due to the strong correlations of the fitted parameters at extreme forward angles. For that reason, until more precise forward angle data of π^0 and η photoproduction from the proton are not available, we consider our analysis suitable for the interpretation of the elementary cross sections. In fact, as we have shown in a recent work dedicated to incoherent π^0 photoproduction from carbon [41], the contribution of Regge cuts is negligible in the nuclear cross section, which is highly sensitive to short-range correlations and meson-nucleus FSI. It is worth mentioning, however, that the predictions from Ref. [39] for the neutron cross section are extremely useful for possible improvements in the analysis, since one can disentangle the isoscalar and isovector contributions of the amplitudes.

III. PHOTOPRODUCTION FROM COMPLEX NUCLEI

A. The cascade approach

The MCMC intranuclear cascade model consists of a semiclassical transport calculation that describes the dynamics of a nuclear reaction via a time-dependent multicollisional Monte Carlo algorithm. The model can be applied for hadron- and photon-induced nuclear reactions, as far as we can neglect the effect of the other nucleons during the first interaction mechanism (IA). For high-energy nuclear incoherent (NI) photoproduction processes, the photon is supposed to interact with a single nucleon and the rest of the nuclear wave function Ψ_{A-1} works as an expectator. The two outgoing particles from the photoproduction vertex (the struck nucleon and the photoproduced meson) are strongly susceptible to interact with the other nucleons, with high probability of producing additional mesons via FSI. These two trajectories can be treated semiclassically and consist of two correlated cascade branchings. The amount of absorption of the primary meson photoproduction flux depends very critically on the photoproduction mechanism itself and also on the dynamics of the excited nuclear system. Such complicated process is generally treated using event generators that account for meson and nucleon multiplicities and gross features of physical observables. These statistical approaches are convenient for the description of the general behavior of the nuclei, since they can be constructed and sometimes adjusted to reproduce the bulk properties of high-energy nuclear reactions. Nevertheless, the advent of high-precision experiments using tagged photon beams and next generation detectors demand a state-of-the-art calculation to account for the inelastic NI

background. Such background is highly dependent on the photoproduction mechanism (Sec. II) and also on several nuclear effects, such as photon shadowing, Pauli blocking, meson absorption, and rescattering back to forward angles, among others. In Sec. II we have proposed a Regge model to account for the initial photoproduction mechanism, which works as the cascade trigger. In this section we present the basic features of the MCMC model to account for the nuclear effects and to deliver accurate information about the angular distributions and the energy spectra of the photoproduced mesons.

B. The nuclear ground state

The positions of the bound nucleons in the Monte Carlo algorithm are distributed using nuclear densities appropriate for light and heavy nuclei. For light nuclei, such as beryllium and carbon, we adopted a shell-model distribution [29]:

$$N(r) = \frac{4}{(a_0\sqrt{\pi})^3}\left(1+\frac{\delta r^2}{a_0^2}\right)\exp\left(\frac{-r^2}{a_0^2}\right), \tag{15}$$

where $a_0 = 1.71$ fm for Be and 1.65 fm for C with $\delta = \frac{1}{6}(A-4)$. For intermediate and heavy nuclei, we have used a Woods-Saxon distribution [29]:

$$N(r) = \frac{N_0}{\exp\left[\frac{(r-c)}{z_1}\right]+1}, \tag{16}$$

where $c = 1.12A^{1/3}$ and $z_1 = 0.545$ fm.

Another important physical constraint to build up a realistic nuclear ground state is the momentum distribution (MD) of the bound nucleons. Since we are specifically concerned with high-precision relativistic kinematics, we have to take into account very accurately the initial state of the struck nucleon. Furthermore, the Pauli blocking mechanism plays an essential role for low momentum transfer and small differences in the MD parametrizations drastically affect the shape of the NI cross sections at small angles.

For intermediate and heavy nuclei, the Fermi gas model is known to work reasonably well and we adopted the uniform distribution in momentum space:

$$W_F(p_N)d^3p_N = \frac{3}{4\pi}\frac{p_N^2}{p_F^3}dp_N\sin(\theta_p)\,d\theta_p d\varphi_p, \tag{17}$$

where p_F is the Fermi momentum and θ_p and φ_p the angular variables defining the direction of the three-momentum of the nucleon $\mathbf{p}_N$.

In contrast with the infinite nuclear matter approximation which works reasonably well for intermediate and heavy nuclei, the MD for light nuclei can be explored using knock-out reactions, such as quasielastic $(e, e'p)$. The missing energy E_m and missing momentum $\mathbf{p}_m$ can be written in the form:

$$E_m = \omega - T_p - T_{A-1}, \tag{18}$$

$$\mathbf{p}_m = \mathbf{p}'_N - \mathbf{q}, \tag{19}$$

where $\mathbf{p}'_N$ and T_p are the momentum and kinetic energy of the outgoing proton and T_{A-1} the kinetic energy of the residual nucleus. The energy and momentum of the virtual photon are ω and $\mathbf{q}$, respectively. In the plane-wave impulse approximation (PWIA), the fivefold differential $(e, e'p)$ cross section can be factorized in the form [42]:

$$\sigma_{ee'p} = \frac{d^5\sigma}{d\Omega_e d\Omega_p dE_p} = K\sigma_{ep}|\phi_\alpha(\mathbf{p}_m)|^2, \tag{20}$$

where $K = \mathbf{p}'_N E_p$, σ_{ep} is the off-shell electron-proton-scattering cross section [43], and $\phi_\alpha(\mathbf{p}_m)$ is the wave function in momentum space of the quantum state α, which can be approximated by a single-particle bound-state wave function. The factorization presented in (20) does not hold if we take into account the distortion effects of the incident electron and outgoing proton and electron. In spite of this, one can still define the reduced cross section $\rho_{ee'p}(\mathbf{p}_m)$ by the ratio between the measured cross section and the electron-proton cross section:

$$\rho_{ee'p}(\mathbf{p}_m) = \frac{\sigma_{ee'p}}{K\sigma_{ep}}. \tag{21}$$

So, by measuring $\sigma_{ee'p}$, we can calculate the distorted momentum distribution $\rho_{ee'p}(\mathbf{p}_m)$, which in PWIA is the squared Fourier transform of the radial wave function.

Obviously the distortion effects on the incoming and outgoing waves depend very critically on the reaction mechanism. These distortions do not permit a model-independent result for the true MD for light nuclei; the main focus of the present analysis. The true MD is the undistorted spectral function integrated in missing energies and is not achievable by proton knock-out experiments. For this reason, we have adopted the PWIA of Ref. [42] as the reference input of the s and p shells MD for light nuclei, where we have assumed the spectroscopic factors $S = 2J + 1$. These momentum distributions, together with the accurate information about the Fermi momentum in light nuclei [44], allow a phenomenological analysis of the spin-orbit coupling during photoproduction. This approach takes advantage of the Monte Carlo method and circumvents the technical difficulties related with the spectral function in actual nuclei. We have also investigated the sensitivity of the cascade results using empirical (distorted) momentum distributions from several nucleon knock-out experiments (see Table 1 from Ref. [45]). An extensive review of the proton knock-out data for light nuclei can be found in Ref. [42] and references therein.

C. Photon shadowing in high-energy photon-nucleus interactions

The direct coupling of high-energy photons with vector mesons propitiates a phenomenological analogy between photon- and hadron-induced nuclear reactions. The main hypothesis of the VMD model is that the physical photon state can be decomposed into a bare and a hadronic component, where the former is not expected to interact with hadrons. So, the photon state is assumed to be given by [46]:

$$|\gamma\rangle \cong \sqrt{Z_3}\,|\gamma_B\rangle + \sqrt{\alpha}\,|h\rangle\,, \tag{22}$$

where the factor Z_3 is introduced for the normalization of $|\gamma\rangle$. One important constraint of the theory is that both $|\gamma_B\rangle$ and $|h\rangle$ have the same quantum numbers ($J^{\rm PC} = 1^{--}$) and the same three-momentum of the physical photon. The assumption that the hadronic state $|h\rangle$ is solely attributed to the vector mesons ρ, ω, and ϕ is one of the main restrictions of the VMD model and is also employed in the present analysis. Considering only the low-mass components of the photon and a narrow resonance state, we may write $\sqrt{\alpha}|h\rangle$ as a superposition of vector-meson states:

$$\sqrt{\alpha}|h_s\rangle_{\rm res} = \sum_V \frac{e}{f_V}|V\rangle, \tag{23}$$

where $\frac{e}{f_V}$ is our choice of normalization for real photons [46] and the label s indicates that such approximation is valid only for low-mass constituents. For higher-mass components, however, the interaction of the vector mesons with hadrons is typically *short ranged* and the hadronic photon behaves similarly as a bare photon without substantial shadowing. Assuming that the bare photon does not interact (VMD), we may connect the scattering amplitudes for high-energy $\gamma N \to X$ processes to analogous amplitudes of vector-meson scattering $VN \to X$ using the S matrix:

$$\langle X|S|\gamma N\rangle = \sum_V \frac{e}{f_V}\langle X|S|VN\rangle. \tag{24}$$

Employing the diagonal approximation and using (24), we may write the total photoabsorption cross section in hadrons $\sigma_{\gamma N}$ due to vector mesons in the form:

$$\sigma_{\gamma N} = \sum_V \frac{e^2}{f_V^2}\sigma_{VN}, \tag{25}$$

where σ_{VN} is the total VN cross section. Taking the coupling constants and the VMD model II of Table XXXV of Ref. [46], we have:

$$\sigma_{\rho N} = \sigma_{\omega N} = 19.1\left[1 + \frac{0.766}{\sqrt{p({\rm GeV}/c)}}\right]{\rm mb} \quad \text{and} \tag{26}$$

$$\sigma_{\phi N} = 12\ {\rm mb}. \tag{27}$$

Inserting Eqs. (26) and (27) into (25) and using a nonshadowed (NS) component of $\sigma_{\gamma N}^{\rm NS} = 24.5\ \mu$b, we have:

$$\sigma_{\gamma N}^{\rm Total}(p) = 19.1e^2\left(\frac{1}{f_\rho^2} + \frac{1}{f_\omega^2}\right)\left[1 + \frac{0.766}{\sqrt{p({\rm GeV}/c)}}\right] + \frac{12.0e^2}{f_\phi^2} + 24.5\,\mu{\rm b}. \tag{28}$$

Equation (28) provides information about the total hadronic cross section and the relative contributions of the vector mesons and the nonshadowed component:

$$R_V = \frac{\frac{e^2}{f_V^2}\sigma_{VN}}{\sigma_{\gamma N}^{\rm Total}}, \qquad R_{\rm NS} = \frac{24.5\mu{\rm b}}{\sigma_{\gamma N}^{\rm Total}}. \tag{29}$$

The total hadronic cross section was measured in the energy interval $3.5 \leqslant k \leqslant 5.4$ GeV ($\sigma_{\gamma p}^{\rm Total} = 116 \pm 17\ \mu$b) [47] and also at 7.5 GeV ($\sigma_{\gamma p}^{\rm Total} = 126 \pm 17\ \mu$b) [48]. The results obtained with Eq. (28) are in nice agreement with the measured values ($\sigma_{\gamma p}^{\rm Total} = 123.6\ \mu$b for $p \simeq 4.5$ GeV and $\sigma_{\gamma p}^{\rm Total} = 117.9\ \mu$b for $p \simeq 7.5$ GeV).

Another important step for the evaluation of the shadowing effect for photonucleus interactions is the concept of *formation time*, which is the time interval that the physical photon is *momentarily in a vector-meson state*. Shadowing effects are expected to take place if the *formation time* is long enough to allow the virtual hadrons to undergo collisions deep in the nuclei as if they were real hadrons. We can estimate the *formation time* of a vector meson with mass m_V using the uncertainty principle:

$$t_f \sim \left|\frac{1}{k - \sqrt{k^2 + m_V^2}}\right|. \tag{30}$$

The mass of the vector meson is sampled in the MC assuming a Lorentzian distribution and the vector meson ρ as the reference ($R_\rho \sim 0.7$):

$$W(m_V) = \frac{1}{2\pi}\frac{\Gamma_\rho}{(m_V - m_\rho)^2 + \left(\frac{\Gamma_\rho}{2}\right)^2}, \tag{31}$$

with $m_\rho = 769.3$ MeV and $\Gamma_\rho = 150.2$ MeV. The corresponding values of t_f are then distributed combining Eqs. (30) and (31). From a direct inspection of Eq. (30), we note that t_f increases with higher photon energies and lower vector-meson masses. The energy dependence of t_f affects the photon ability to interact with hadrons. The higher is the photon energy, the stronger is its attenuation deep in the nuclei. The relationship between ct_f and the size of the nucleus also originates a much steeper decrease of the photoabsorption cross section for heavy nuclei at higher energies, in comparison with light nuclei.

The evaluation of the shadowing effect is performed using the MCMC cascade model in a straightforward approach. The nuclear photoabsorption cross section is expected to be proportional to the single nucleon cross section such that

$$\sigma_{\gamma A}^{\rm Total} = A_{\rm eff}\sigma_{\gamma N}^{\rm Total}, \tag{32}$$

where $A_{\rm eff}$ is the effective number of nucleons that contribute to the reaction. The values of $A_{\rm eff}$ provide information about the nuclear response and the ratio $\frac{A_{\rm eff}}{A}$ gives the amount of photon shadowing considering the total nuclear photoabsorption mechanism. For the case of nondiffractive meson photoproduction, however, the values of $A_{\rm eff}$ also include the effects of FSI of the photoproduced mesons. Consequently, the values of $\frac{A_{\rm eff}}{A}$ obtained in this section refer to the initial photoabsorption process only such that $A_{\rm eff} \equiv A_{\rm eff}^{\rm abs}$.

The factor $A_{\rm eff}^{\rm abs}$ can be calculated using the information about the nuclear transparency to the *hadronic photon* obtained under the framework of the cascade model. In this approach, we can calculate $A_{\rm eff}^{\rm abs}$ using the separation of (25) and the additional NS contribution:

$$A_{\rm eff}^{\rm abs} = AR_{\rm NS} + AR_\rho {\rm T}_{\gamma\rho} + AR_\omega {\rm T}_{\gamma\omega} + AR_\phi {\rm T}_{\gamma\phi}, \tag{33}$$

where $T_{\gamma V}$ represents the nuclear transparency of the *hadronic photon* assuming a direct coupling to its hadronic components ρ, ω, and ϕ. Since in our model $\sigma_{\rho N} = \sigma_{\omega N}$, we have $T_{\gamma\rho} = T_{\gamma\omega}$. The nuclear transparencies are then calculated as a function of the nuclear densities as follows:

$$T_{\gamma V} = \frac{4\pi}{A} \int T_{\gamma V}(r) N(r) r^2 dr, \tag{34}$$

where $T_{\gamma V}(r)$ is the transparency of the *hadronic photon* as a function of the radial distance. Obviously for nonshadowed photoabsorption, we have $T_{\gamma V}(r) = 1$ and Eq. (33) gives $A_{\rm eff}^{\rm abs} = A$. The nuclear transparency of the *hadronic photon* is calculated as a function of the radial distance considering that the incoming photon couples with the vector mesons with impact parameters uniformly distributed in the area of a disk perpendicular to the photon direction (z axis). For each cascade run, the vector-meson mass m_V and the *formation time* t_f are distributed according to Eqs. (30) and (31), conserving the three-momentum of the incoming photon. The *formation time* t_f starts when the vector meson and the struck nucleon reach their minimal relative distance and the primary VN collisions are collected. The nuclear transparencies obtained under the cascade framework are shown in Fig. 4, where we have included the results from Be, C, Cu, and Pb from 3.2 to 8.6 GeV. The vector-meson *formation time* t_f plays an important role for the evaluation of the transparencies. For instance, for larger nuclei, the amount of photon shadowing increases with ct_f. On the other hand, for light systems, the transparencies tend to an asymptotic value above approximately 6 GeV, since any increase in ct_f will not increase the fraction of the nuclear volume illuminated by the vector meson. This argument also explain why the *hadronic photon* transparencies are higher for heavier nuclei at lower energies, since the magnitude of ct_f is much lower than the nuclear size.

D. Pauli blocking in the MCMC model: A time-dependent nonstochastic approach

Short-range correlations in nuclear matter play an important role for the accurate determination of meson angular distributions at extreme forward angles. The Pauli suppression reduces the cross sections in the forward direction (meson photoproduction) and also dictates the dynamics of secondary meson-nucleon scatterings (meson-nucleus FSI) during the cascade process. As we have shown in a work dedicated to the quasideuteron channel [49], the evaluation of the Pauli blocking is crucial for low-energy photonuclear reactions. In this work, a nonstochastic Pauli blocking was implemented propitiating a time-dependent analysis of multiple particle-hole excitations during the cascade process. The method is completely new and provides a more rigorous formalism to address short-range correlations in nuclear matter in comparison with the statistical approaches employed in some refined transport calculations [10], as well as in other cascade models, like the sophisticated Liège INC model [50]. Similarly with the scenario found in low-energy nuclear reactions, forward-angle meson photoproduction processes are also strongly sensitive to the Pauli blocking mechanism due to the typical

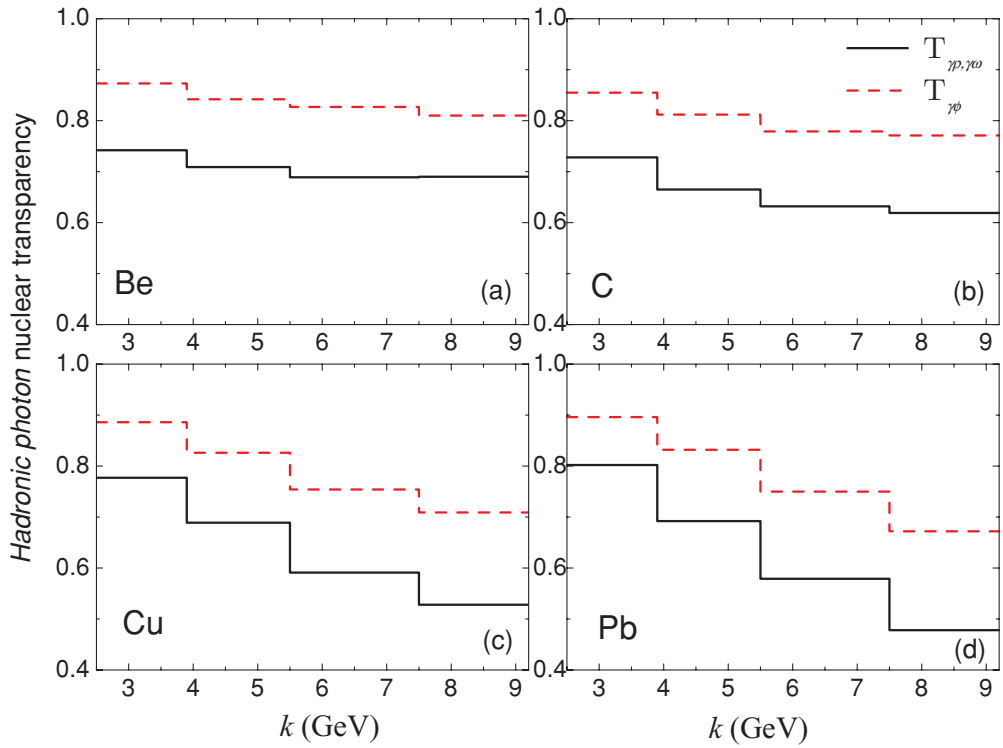

FIG. 4. (Color online) *Hadronic photon* nuclear transparencies from the MCMC model for (a) Be, (b) C, (c) Cu, and (d) Pb within 3.2 to 8.6 GeV. The dashed red lines represent the transparencies assuming the coupling of the incoming photon with the vector meson ϕ and the solid black lines refer to the coupling with ρ or ω.

small-momentum-transfer regime. Furthermore, the Pauli blocking suppression depends on the initial nucleon momentum and also on the meson-scattering angle, making the MC approach a convenient framework to address such a complicated process.

The Pauli-suppression factor can also be calculated analytically considering the Fermi gas model or an independent particle model with harmonic oscillator (HO) wave functions. The former is expected to work properly for intermediate and heavy nuclei, while the latter is useful for the description of finite nuclei effects in light and double magic nuclei, such as ^{16}O. A detailed review about neutral pion photoproduction from complex nuclei up to 900 MeV and the Pauli blocking factors can be found in Ref. [3]. In this approach, the Pauli-suppression factor for intermediate and heavy nuclei is given by

$$1 - G(q_t) = \frac{3}{4}\left(\frac{q_t}{p_F}\right) - \frac{1}{16}\left(\frac{q_t}{p_F}\right)^3 \quad \text{for} \quad q_t < 2p_F \quad \text{and} \\ = 1 \quad \text{for} \quad q_t > 2p_F, \tag{35}$$

where p_F is the Fermi momentum with $q_t \sim k\theta$. For light nuclei, the following expression was obtained:

$$1 - G(q_t) = 1 - \left[1 + \left(\frac{q_t}{2\kappa}\right)^4\right] \exp\left(\frac{-q_t^2}{2\kappa^2}\right), \tag{36}$$

where $\kappa^2 = \frac{15}{4R^2} \simeq 0.019\ (\mathrm{GeV}/c)^2$.

The MCMC model, on the other hand, consists of an appropriate tool for the accurate determination of the Pauli blocking suppression factor. Equations (35) and (36) were derived using closure approximation without any specification about the photoproduction operator. The MCMC model also requires closure, since the NI amplitude for meson photoproduction from the nucleus is obtained as an incoherent sum of single nucleon amplitudes, but it is still possible to include the dynamical information for the elementary photoproduction during the evaluation of the Pauli-suppression factor. This powerful Monte Carlo method provides a more accurate calculation of the Pauli blocking, since it accounts for the underlying dynamics of the photoproduction mechanism. For the case of heavy nuclei one should expect small differences between Eq. (35) and the MCMC model, since in both cases the MD of the nucleons are taken from the Fermi gas model. For the case of light nuclei, on the other hand, more significant differences between the MCMC model and the calculations presented in Ref. [3] should be expected due to the realistic MD used in the former. The Pauli blocking factor in the MCMC model—herein denoted $f_{\mathrm{PB}}(k,\theta)$—is easily obtained by the ratio between Pauli-allowed and the total number of events, after distributing the meson production angle in the center of mass of the s channel using Eq. (8). So, the total cross section after the inclusion of the Pauli principle $(\frac{d\sigma}{d\Omega})^{\mathrm{PB}}$ can be written as:

$$\left(\frac{d\sigma}{d\Omega}\right)^{\mathrm{PB}} = f_{\mathrm{PB}}(k,\theta)\left(\frac{d\sigma}{d\Omega}\right)^{\mathrm{PWIA}} = A f_{\mathrm{PB}}(k,\theta)\left(\frac{d\sigma_n}{d\Omega}\right). \tag{37}$$

Figure 5 shows the results of the Pauli blocking factors for π^0 photoproduction at 5.2 GeV from carbon (a) and lead (b) obtained via the MCMC model using the photoproduction mechanism of Eq. (8) (solid black lines). The predictions from the HO model [Eq. (36)] and the Fermi gas model [Eq. (35)] are given by the red dashed lines, where we have used a Fermi momentum of 279 MeV/c for lead. As previously expected, the result from the MCMC model for light nuclei differs substantially from the predictions given by the HO model. There are two distinct structures in $f_{\mathrm{PB}}(k,\theta)$ for carbon at $\sim$0.5° and $\sim$3.0° associated with the dominant contributions from the p and s shells, respectively. Furthermore, the Pauli suppression obtained in the MCMC model (assuming a Fermi momentum of 221 MeV/c for carbon [44]) is much weaker than the one obtained by the double magic configuration of the HO model. Obviously the HO potential of Ref. [3] is expected to work properly for nuclei with closed s and p shells, such as the working example ^{16}O presented there. In this model, the $p_{3/2}$ and $p_{1/2}$ states are degenerated, propitiating an analytical expression for $G(k,\theta)$. Nevertheless, for the case of nonclosed p-shell nuclei, such as Be and C, the spin-orbit term plays an essential role, making the HO approximation a crude estimate in comparison with the accurate MD used in the MCMC model. The result for heavy nuclei is also less restrictive than the prediction from the Fermi gas as a consequence of the forward-peaked elementary photoproduction cross section. The result of the MCMC model for lead assuming isotropic photoproduction (dotted blue line) agrees remarkably well with the prediction from the Fermi gas model, as previously expected. It is clear that the Pauli blocking factor depends on the photoproduction mechanism, since the later is much more favorable for meson photoproduction at forward angles, softening the Pauli suppression.

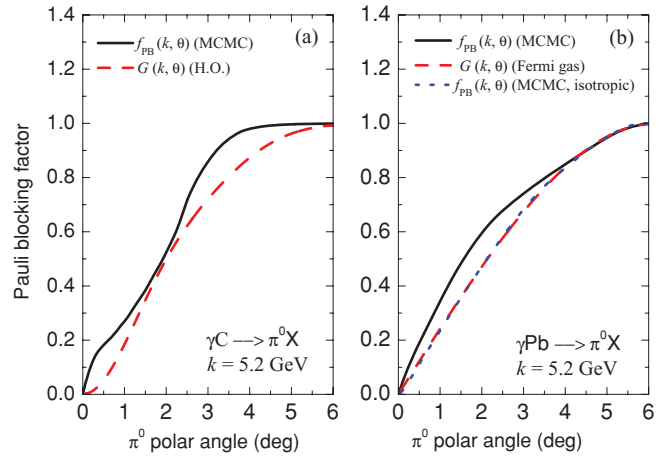

FIG. 5. (Color online) Pauli blocking factors for π^0 photoproduction from (a) carbon and (b) lead at 5.2 GeV. The solid black lines show the results from the MCMC model taking into account the photoproduction mechanism of Eq. (8). The dashed red lines are the predictions from the HO (a) and Fermi gas (b) models, while the dotted blue line refers to the cascade model predictions for lead assuming isotropic photoproduction.

Additionally to the issue of Pauli suppression during meson photoproduction, short-range correlations dictate the dynamics of the nuclear reaction due to binary meson-nucleon scattering processes. As will be presented in the next section,

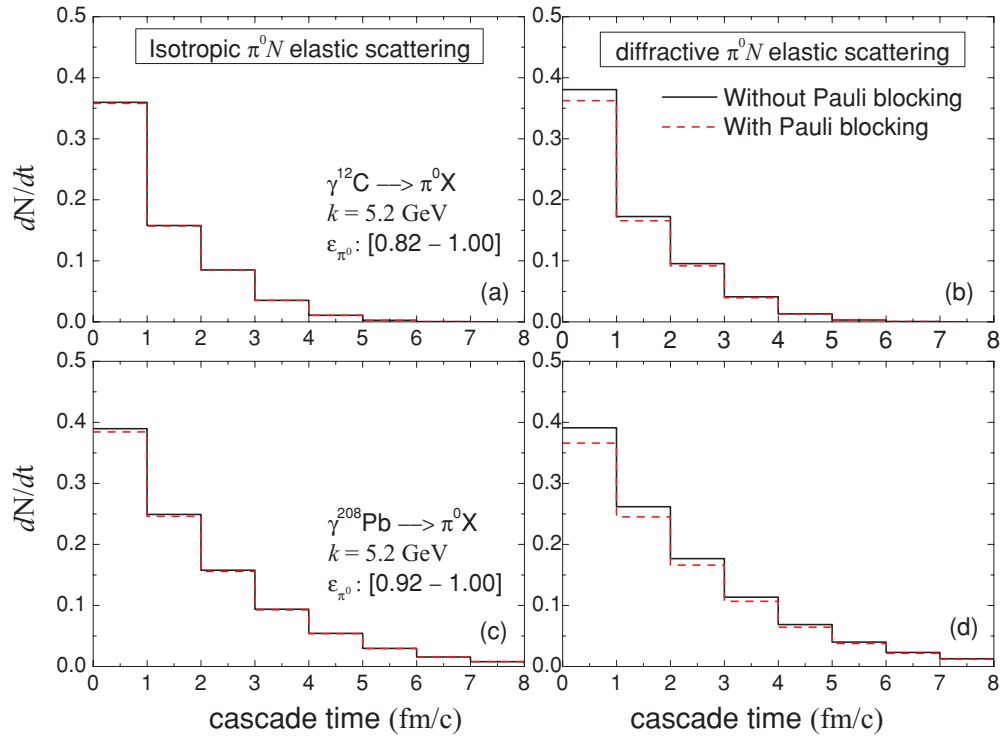

FIG. 6. (Color online) Time derivative of the average number of $\pi^0 N$ scatterings with (dashed-red) and without (solid black) Pauli blocking at 5.2 GeV for carbon (upper panels) and lead (lower panels). The left/right plots assume isotropic/diffractive elastic $\pi^0 N$ scattering. The elasticity cuts on the π^0 energy were taken as 0.82 for carbon and 0.92 for lead.

the elastic meson-nucleon channel is of the order of 20% of the total meson-nucleon cross section, exhibiting a typical diffractive behavior. Therefore, the elastic channel is largely dominated by low-momentum transfer, making the evaluation of the Pauli blocking mechanism a critical step in the cascade process.

In order to evaluate the influence of the Pauli principle during secondary scatterings, we have run the cascade model with and without the Pauli blocking, collecting binary meson-nucleon collisions as a function of the intranuclear cascade time. The final results are extremely sensitive to the kinematical cuts in the meson elasticity ($\varepsilon_P = \frac{E_P}{k}$), which represents a minimum energy cutoff value to interrupt the cascade process. The higher is the meson elasticity ($E_P \approx k$), the lower is the scattering angle and the higher is the fraction of Pauli-blocked events. For extremely inelastic events ($\varepsilon_P \ll 1$), the meson ability to interact is strongly reduced and the fraction of blocked events also increases. A typical result for the time derivative of the average number of $\pi^0 N$ scatterings ($\frac{dN}{dt}$) during a cascade at $k = 5.2$ GeV is presented in Fig. 6 for carbon (upper plots) and lead (lower plots). The calculations assume both isotropic $\pi^0 N \to \pi^0 N$ scattering (left plots) and a more realistic $\pi^0 N \to \pi^0 N$ scattering (right plots) taken from $\pi^{+/-} p \to \pi^{+/-} p$ data (see the next section). The solid black/dashed red lines represent $\frac{dN}{dt}$ neglecting/including the Pauli blocking. The total number of scatterings is obtained by the integral $\int \frac{dN}{dt} dt$ and the ratio between the Pauli-allowed and the total number of scatterings gives the fraction of unblocked events. These fractions are 0.995 (0.956) for carbon and 0.983 (0.938) for lead, taking into account isotropic (diffractive) $\pi^0 N$ elastic scattering. The results using the diffractive elastic scattering show that the Pauli principle affects 5 to 6% of all the binary events during the cascade stage. Considering that the Pauli principle affects more significantly the elastic channel, we can estimate that approximately 25% of the elastic $\pi^0 N$ scatterings are being blocked, since this mechanism accounts for approximately 20% of the total $\pi^0 N$ cross section.

E. Meson-nucleus final-state interactions

The calculation of the FSI of the photoproduced mesons with the nucleus is the main issue for the determination of the NI cross section. The huge amount of open channels requires a powerful tool, based on a sophisticated Monte Carlo algorithm, to address the dynamics of such complicated system. The main disadvantage of the Glauber model for the calculation of the absorption and rescattering effects is that it does not account for energy losses during secondary scatterings and also includes short-range correlations using phase-space considerations. However, for meson photoproduction at extreme forward angles, *soft* meson-nucleon scatterings are most likely to occur, making the analysis of the Pauli blocking and FSI very sensitive to the meson-nucleon kinematics and dynamics. The kinematics has to take into account the energy losses during the cascade process and also the realistic MD for the bound nucleons, while the dynamics should incorporate, as accurately as possible, the s and t dependence of the secondary scattering mechanism.

Table II presents the meson-nucleon channels for π^0 photoproduction considered in the MCMC cascade. The

TABLE II. Meson-nucleon scattering channels considered in the MCMC model. The input channels are represented by the first line, while the output channels are represented by lines 1 to 22. The last line represents the mechanism of pion absorption by a nucleon-nucleon pair. Details in the text.

Out ⇓ \in ⇒	$\pi^0 p$	$\pi^+ p$	$\pi^- p$	$\pi^0 n$	$\pi^+ n$	$\pi^- n$
1	$\pi^0 p$	$\pi^+ p$	$\pi^- p$	$\pi^0 n$	$\pi^+ n$	$\pi^- n$
2	$\Delta(1232)^+$	$\Delta(1232)^{++}$	$\Delta(1232)^0$	$\Delta(1232)^0$	$\Delta(1232)^+$	$\Delta(1232)^-$
3	$N^*(1520)^+$	–	$N^*(1520)^0$	$N^*(1520)^0$	$N^*(1520)^+$	–
4	$N^*(1680)^+$	–	$N^*(1680)^0$	$N^*(1680)^0$	$N^*(1680)^+$	–
5	$\Delta(1950)^+$	$\Delta(1950)^{++}$	–	$\Delta(1950)^0$	–	$\Delta(1950)^-$
6	$\pi^+ n$	–	$\pi^0 n$	$\pi^- p$	$\pi^0 p$	–
7	$2\pi^0 p$	$\pi^0\pi^+ p$	$\pi^0\pi^- p$	$2\pi^0 n$	$\pi^0\pi^+ n$	$\pi^0\pi^- n$
8	–	–	$2\pi^0 n$	–	$2\pi^0 p$	–
9	$3\pi^0 p$	$2\pi^0\pi^+ p$	$2\pi^0\pi^- p$	$3\pi^0 n$	$2\pi^0\pi^+ n$	$2\pi^0\pi^- n$
10	$2\pi^0\pi^+\pi^- p$	$\pi^0 2\pi^+\pi^- p$	$\pi^0\pi^+ 2\pi^- p$	$2\pi^0\pi^+\pi^- n$	$\pi^0 2\pi^+\pi^- n$	$\pi^0\pi^+ 2\pi^- n$
11	$3\pi^0\pi^+ n$	$2\pi^0 2\pi^+ n$	$2\pi^0\pi^+\pi^- n$	$3\pi^0\pi^- p$	$2\pi^0\pi^-\pi^+ p$	$2\pi^0 2\pi^- p$
12	$\pi^0\pi^+ n$	$2\pi^+ n$	$\pi^+\pi^- n$	$\pi^0\pi^- p$	$\pi^-\pi^+ p$	$2\pi^- p$
13	$\pi^0\pi^+\pi^- p$	$2\pi^+\pi^- p$	$\pi^+ 2\pi^- p$	$\pi^0\pi^+\pi^- n$	$2\pi^+\pi^- n$	$\pi^+ 2\pi^- n$
14	$\pi^0 2\pi^+\pi^- n$	$3\pi^+\pi^- n$	$2\pi^+ 2\pi^- n$	$\pi^0\pi^+ 2\pi^- p$	$2\pi^+ 2\pi^- p$	$3\pi^-\pi^+ p$
15	$2\pi^0\pi^+ n$	$\pi^0 2\pi^+ n$	$\pi^0\pi^+\pi^- n$	$2\pi^0\pi^- p$	$\pi^0\pi^+\pi^- p$	$\pi^0 2\pi^- p$
16	–	–	$3\pi^0 n$	–	$3\pi^0 p$	–
17	$\pi^0 2\pi^+ 2\pi^- p$	$3\pi^+ 2\pi^- p$	$2\pi^+ 3\pi^- p$	$\pi^0 2\pi^+ 2\pi^- n$	$3\pi^+ 2\pi^- n$	$2\pi^+ 3\pi^- n$
18	$\pi^0 3\pi^+ 2\pi^- n$	$4\pi^+ 2\pi^- n$	$3\pi^+ 3\pi^- n$	$\pi^0 2\pi^+ 3\pi^- p$	$3\pi^+ 3\pi^- p$	$2\pi^+ 4\pi^- p$
19	$2\pi^0 2\pi^+ 2\pi^- p$	$\pi^0 3\pi^+ 2\pi^- p$	$\pi^0 2\pi^+ 3\pi^- p$	$2\pi^0 2\pi^+ 2\pi^- n$	$\pi^0 3\pi^+ 2\pi^- n$	$\pi^0 2\pi^+ 3\pi^- n$
20	$4\pi^0 p$	$3\pi^0\pi^+ p$	$3\pi^0\pi^- p$	$4\pi^0 n$	$3\pi^0\pi^+ n$	$3\pi^0\pi^- n$
21	$3\pi^0\pi^+\pi^- p$	$2\pi^0 2\pi^+\pi^- p$	$2\pi^0\pi^+ 2\pi^- p$	$3\pi^0\pi^+\pi^- n$	$2\pi^0 2\pi^+\pi^- n$	$2\pi^0\pi^+ 2\pi^- n$
22	$(+n) \to pn$	$(+n) \to pp$	$(+n) \to nn$	$(+p) \to np$	$(+p) \to pp$	$(+p) \to nn$

entrance channels are given by binary collisions with one pion (π^0, π^+, π^-) and one nucleon (p, n). Collisions of the type πN, πN^*, $\pi\Delta$, NN, NN^*, and $N\Delta$ are taken into account, but collisions between pairs of pions are not considered due to a much lower pion density. There is a huge amount of important channels in high-energy photoproduction processes and a great number of additional mesons are likely to be produced via FSI. Figure 7 presents the energy dependence incorporated in the MCMC code for the $\pi^0 p(n) \to X$ channels. The cross sections for the output channels (1 trough 22 in Table II) were estimated combining the symmetry properties of isospin and time reversal of the strong interactions and the results for charged pions; usually constrained by the experimental data.

A typical entrance channel for $\pi^+ p \to X$ is presented in Fig. 8 in comparison with the PDG total cross section [25], where the magenta solid line represents the sum of all processes included in the MCMC model. Such procedure allowed the inclusion of approximately 95% (85%) of the relevant channels for $\pi^+ p \to X$ and 85% (55%) for $\pi^- p \to X$ at 6 GeV (12 GeV). The production of vector mesons and strange particles in secondary scatterings is neglected in our analysis, explaining our limitations with the neutral channel $\pi^- p \to X$ at higher energies. However, as will be discussed later, the π^0-nucleon interaction probability is considered in the MCMC model taking into account the total cross section $\sigma_{\pi^0 N \to \text{Total}}$, instead of the sum of all channels from Table II. The total cross section, on the other hand, is assumed to be the average $(\sigma_{\pi^+ p \to \text{Total}} + \sigma_{\pi^- p \to \text{Total}})/2$. The cross sections $\sigma_{\pi^+ p \to \text{Total}}$ and $\sigma_{\pi^- p \to \text{Total}}$ are then obtained by fitting the available data using the Regge parametrization [51]:

$$\sigma_{\pi^\pm p \to \text{Total}}(s) = Z^{\pi^\pm p} + B \log^2\left(\frac{s}{s_2}\right) + Y^{\pi^\pm p}\left(\frac{s_1}{s}\right)^\eta, \quad (38)$$

with $B = 0.308$ mb, $\sqrt{s_1} = 1$ GeV, $\sqrt{s_2} = 5.38$ GeV [51] and the charge conjugation symmetry $\eta_1 = \eta_2 = \eta \sim 0.49$. The parameters $Z^{\pi^+ p} = 19.29(56)$ mb, $Z^{\pi^- p} = 19.62(31)$ mb,

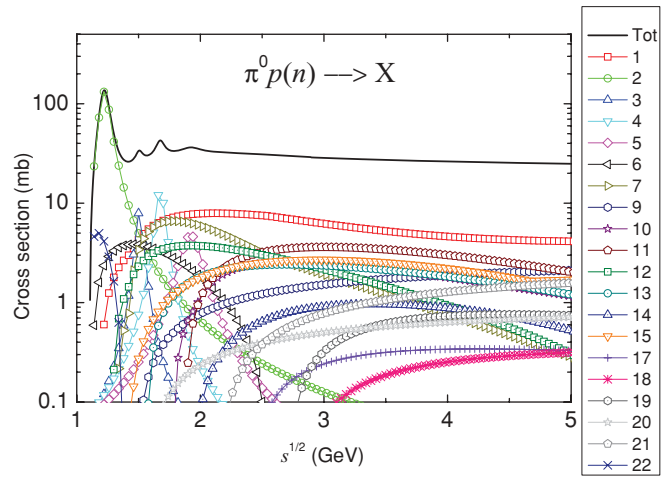

FIG. 7. (Color online) Energy dependence for the $\pi^0 p(n) \to X$ channels included in the MCMC routine. The solid black line represents the total cross section taken as the average $(\sigma_{\pi^+ p \to \text{Total}} + \sigma_{\pi^- p \to \text{Total}})/2$. The output channels (1 to 22) are shown in Table II for the input channels $\pi^0 p$ and $\pi^0 n$.

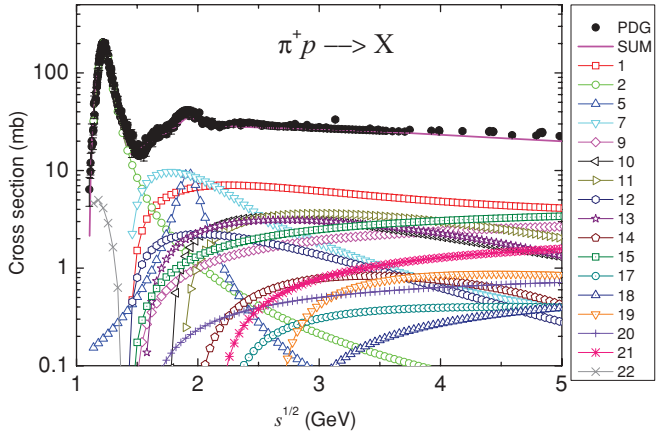

FIG. 8. (Color online) Energy dependence for the $\pi^+ p \to X$ channels included in the MCMC routine versus the PDG data for $\sigma_{\pi^+ p \to \text{Total}}$. The solid magenta line represents the sum of all processes (second column of Table II) for the $\pi^+ p$ scattering included in the algorithm. Details in the text.

$Y^{\pi^+ p} = 23.1(19)$ mb, and $Y^{\pi^- p} = 29.7(10)$ mb were obtained by fitting the $\pi^+ p$ ($\chi^2/\text{DOF} = 1.16$) and $\pi^- p$ data ($\chi^2/\text{DOF} = 0.83$) from 4 to 12 GeV. The results of the fitted cross sections are presented in Fig. 9. Such procedure assures that our best knowledge of the pion-nucleon cross section is considered for the evaluation of the interaction probability, despite our limitations to exhaust the output channels for $\pi^- p \to X$ at higher energies (~12 GeV).

Furthermore, our calculations consider only a single-meson photoproduction mechanism and are not suitable to describe the total meson yield at any arbitrary large angle and low-elasticity regime. The single-meson photoproduction mechanism represents only a fraction (~10%) of the total hadronic cross section [48], restricting our analysis to the quasielastic domain. So the calculations and results that follow for π^0 photoproduction consider only single-meson

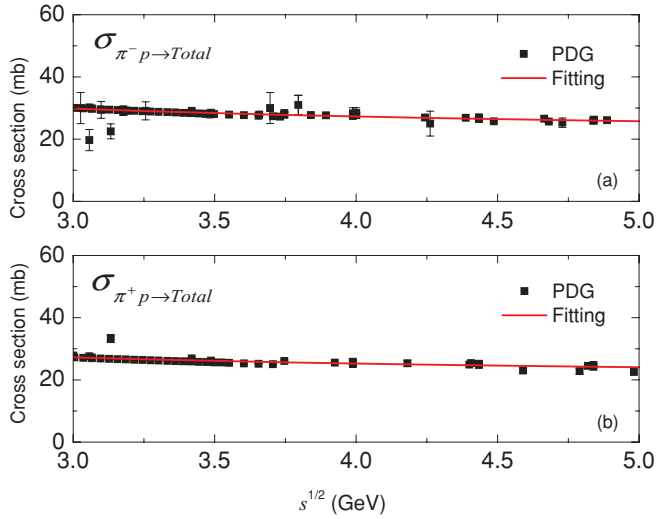

FIG. 9. (Color online) Total cross sections for $\pi^- p$ (a) and $\pi^+ p$ (b) from PDG (data points) in comparison with the parametrization [Eq. (38)] employed in the MCMC model (solid red lines).

photoproduction that subsequently interacts with the bound nucleons in accordance with the elementary processes depicted in Table II. As will be presented in the following sections, the NI photoproduction cross section is forward peaked and largely dominated by quasielastic mesons, making the elasticity cuts a powerful tool for the interpretation of the available data via the MCMC model.

For the case of η photoproduction, on the other hand, we adopted a simpler procedure due to our lack of knowledge on both the total and elastic ηN cross sections. The calculations assumed that $\sigma_{\eta N \to \text{Total}} = C\ \sigma_{\pi^0 N \to \text{Total}}$ and $\frac{\sigma_{\eta N \to \eta N}}{\sigma_{\eta N \to \text{Total}}} = \frac{\sigma_{\pi^0 N \to \pi^0 N}}{\sigma_{\pi^0 N \to \text{Total}}}$, with C representing a multiplicative factor. Due to the absense of absolute cross-section measurements for η photoproduction from complex nuclei it was not possible to estimate the constant C with the help of the MCMC model and the results that follow assume $C = 1$. With this approximation, the total η-nucleon cross section is the sum of the elastic part $\sigma_{\eta N \to \eta N}$ and one absorptive part given by $\sigma_{\eta N \to \text{abs}} = \sigma_{\eta N \to \text{Total}} - \sigma_{\eta N \to \eta N}$.

The elastic $\pi^0(\eta)N \to \pi^0(\eta)N$ channel consists of the most important contribution (~20%) of the total cross section within 4 to 12 GeV and is also the major source of quasi-elastic mesons at the forward direction after secondary scatterings. Other channels can also contribute in the quasielastic domain. For instance, a charged pion photoproduction can contribute to the π^0 yield via a charge-exchange process. Fortunately, the probability for a charge exchange goes to zero above $\sqrt{s} \approx 2.5$ GeV (output channel 6 from Table II and Fig. 7) and these processes can be safely neglected above 4 GeV. On the other hand, the decay of the vector mesons ρ and ω into the π^0 channel can contribute significantly in the hadronic background of neutral pions. Specifically, the channel $\omega \to \pi^0 \gamma$ is expected to play an important role at forward angles due to the combination of three factors: (i) a huge diffractive ω photoproduction in nuclei, (ii) a significant branching ratio for the $\omega \to \pi^0 \gamma$ decay (8.5%), and (iii) a favorable kinematics for the production of high-energy and forward-peaked pions in the $\omega \to \pi^0 \gamma$ decay. The contribution of the $\omega \to \pi^0 \gamma$ decay in the π^0 inelastic cross section (NI plus ω photoproduction) was estimated to be ~5% for carbon and lead at $k = 5.2$ GeV and $\theta_{\pi^0} \sim 4^\circ$.

The differential cross section for elastic $\pi^0(\eta)N \to \pi^0(\eta)N$ scattering was assumed as the average:

$$\left(\frac{d\sigma}{d\Omega}\right)_{\pi^0(\eta)N \to \pi^0(\eta)N} = \frac{1}{2}\left[\left(\frac{d\sigma}{d\Omega}\right)_{\pi^+ p \to \pi^+ p} + \left(\frac{d\sigma}{d\Omega}\right)_{\pi^- p \to \pi^- p}\right], \quad (39)$$

with the cross sections for $\pi^{+(-)} p \to \pi^{+(-)} p$ scattering given by [52]:

$$\left(\frac{d\sigma}{d\Omega}\right)_{\pi^{+(-)} p \to \pi^{+(-)} p} = \frac{\sigma_{\pi^{+(-)} p \to \text{Total}}(p)}{\sigma_{\pi^{+(-)} p \to \text{Total}}(p_0)} \exp(a + bt + ct^2), \quad (40)$$

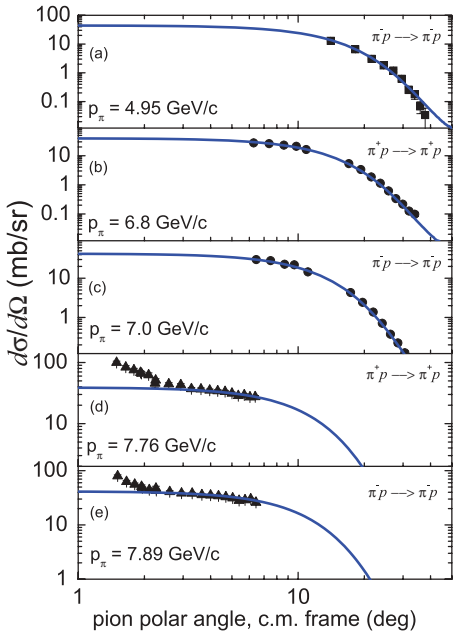

FIG. 10. (Color online) Differential cross section for the elastic $\pi^{+(-)}p \to \pi^{+(-)}p$ scattering (data points) versus the prediction from Eq. (40) (solid blue lines). The data points are from Ref. [53] (squares), Ref. [54] (circles), and Ref. [55] (triangles). Details in the text.

where $p_0 = 20$ GeV/c. The total cross sections $\sigma_{\pi^{+(-)}p\to\text{Total}}$ is calculated from Eq. (38) and can also be approximated by:

$$\sigma_{\pi^+ p\to\text{Total}}(p) = 23.01 + \frac{20.48}{p(\text{GeV}/c)} \tag{41}$$

$$\sigma_{\pi^- p\to\text{Total}}(p) = 24.1 + \frac{26.78}{p(\text{GeV}/c)}, \tag{42}$$

with the parameters a, b, and c taken from Ref. [52].

The differential cross sections for the elastic $\pi^{+(-)}p \to \pi^{+(-)}p$ scattering at several pion momenta are presented in Fig. 10 in comparison with the available data [53–55]. The data at extreme forward angles [55] show an enhancement due to the Coulomb exchange, which is not taken into account in Eq. (40). Fortunately, the elastic $\pi^0(\eta)N \to \pi^0(\eta)N$ channel is not sensitive to the Coulomb term and is safely described by the combination of Eqs. (39) and (40).

IV. RESULTS

A. π^0 photoproduction

1. *Single differential cross sections for incoherent π^0 photoproduction from complex nuclei*

The single differential cross section for incoherent π^0 photoproduction from complex nuclei is calculated combining the elementary photoproduction mechanism described in Sec. II with the nuclear effects delineated in the previous section. The elementary photoproduction constraints the initial polar angle of the photoproduced meson and provides the normalization of the final results. The total cross section from complex nuclei

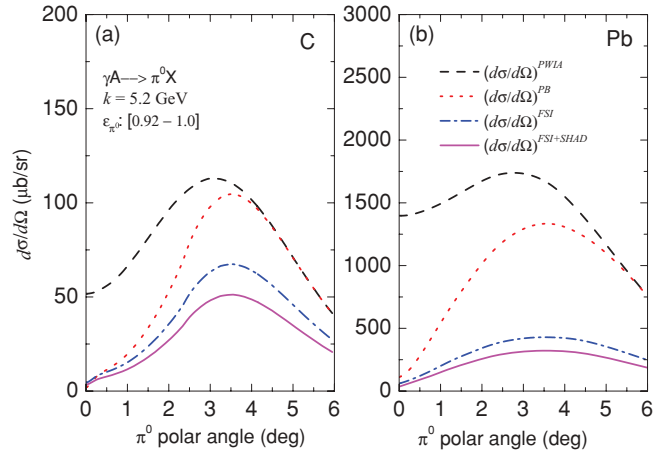

FIG. 11. (Color online) Differential cross section for incoherent π^0 photoproduction from (a) carbon and (b) lead at 5.2 GeV. The dashed black line is the PWIA [Eq. (43)] and the dotted red line includes the Pauli blocking. The results taking into account the FSI are given by the dashed-dotted blue line, while the solid magenta line represents our final results that also include photon shadowing. The calculations assume an elasticity cut on pion energy of 0.92.

neglecting the nuclear effects is simply given by:

$$\left(\frac{d\sigma}{d\Omega}\right)^{\text{PWIA}} = A\left(\frac{d\sigma_n}{d\Omega}\right). \tag{43}$$

The other steps introduce the nuclear effects, such as the Pauli blocking and meson-nucleus FSI. The shadowing effect reduces the cross sections by a factor $\frac{A_{\text{eff}}^{\text{abs}}}{A}$ and is angle independent in our approach (see the previous section).

The predictions of the cascade model for incoherent π^0 photoproduction from carbon and lead at 5.2 GeV are presented in Fig. 11; where we have used an elasticity cut on the pion energy of $\varepsilon_{\pi^0} \geqslant 0.92$. The results of the PWIA [Eq. (43)] are presented by the black dashed lines, while the red dotted lines include the effect of Pauli blocking. The results after the inclusion of FSI are shown by the blue dashed-dotted lines and the final results (including photon shadowing) are given by the solid magenta lines. The Pauli suppression reduces the cross sections at low polar angles and dictates its overall shape. The FSI of the photoproduced mesons also influence the final shape of the cross sections mostly due to the contribution of secondary elastic meson-nucleon scatterings at forward angles. The effects of FSI are almost angle independent above approximately 2° and the attenuation is typically 35% for carbon and 70% for lead. Below ∼2°, the contribution of the elastic meson-nucleon scattering plays an essential role, increasing the cross sections. The effect of photon shadowing is angle independent and reduces the cross sections by the ratio $\frac{A_{\text{eff}}^{\text{abs}}}{A} \sim 0.75$ both for carbon and lead.

The MCMC model results for carbon [Fig. 11(a)] differ in shape and magnitude from the recent results published in Ref. [4]. For instance, at $\theta_{\pi^0} \sim 0^0$, we found ∼2.3 mb instead of ∼1 mb, found in Ref. [4]. Moreover, at approximately 1°, we found 11.5 mb while ∼3 mb is reported in Ref. [4]. The predictions match around 2° (∼28 mb) and also differ at higher angles, where we found ∼49 mb at 4°, in comparison

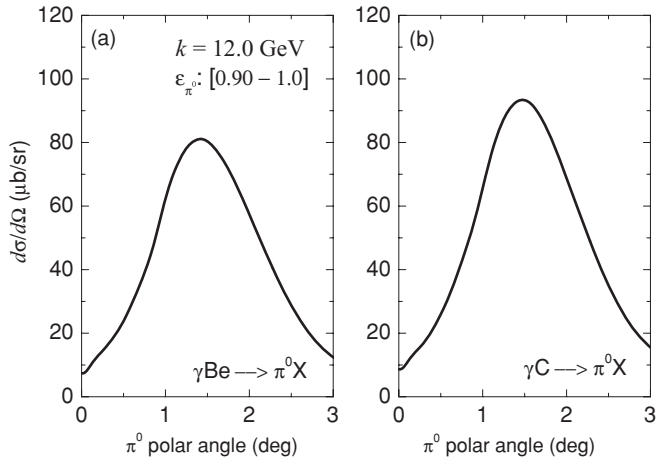

FIG. 12. Differential cross section for incoherent π^0 photoproduction from (a) Be and (b) C at 12.0 GeV. The solid black lines are the final results from the cascade model assuming an elasticity cut of 0.90 on the pion energy.

with ∼62 mb found in Ref. [4]. The higher cross section at low polar angles found in our analysis is probably associated with the elastic $\pi^0 N$ scattering in secondary interactions. Such mechanism is forward peaked (see Fig. 10) and increases the cross sections in the forward direction. The peak angle for the NI cross sections is the same in both calculations (∼3.5°), which are approximately proportional above ∼2.5°. The ratio between the results from Ref. [4] and the MCMC model prediction is typically 1.25 at higher angles. Such difference in magnitude could be associated with the photon shadowing effect ($\frac{A_{\rm eff}^{\rm abs}}{A} \sim 0.75$), which is neglected in Ref. [4]. A further discussion about the magnitude of the NI cross section will be presented later, where we compare the MCMC results with previous measurements from Cornell.

The predictions of the MCMC model at 12 GeV are presented in Figs. 12(a) for beryllium and 12(b) for carbon. The solid black lines show the final results obtained after running the cascade model with an elasticity cut on the pion energy of 0.9. The results cover the existing lack in the theory related with incoherent photoproduction and might be helpful for the delineation of the inelastic background in future experiments dedicated to the extraction of the $\pi^0(\eta) \to \gamma\gamma$ decay width via the Primakoff method (see the discussion below).

2. *Double differential cross sections for incoherent π^0 photoproduction from complex nuclei*

The double differential cross section for incoherent meson photoproduction from complex nuclei is the most convenient observable for the evaluation of the hadronic background at forward angles. Such theoretical prediction propitiates the construction of realistic event generators of the NI mechanism, since it includes the information about the energy losses due to the nuclear excitation either with or without secondary meson-nucleus interactions. Different kinematical cuts may take place in different analyses and the double differential cross section could provide a consistent and convenient tool to match theory and experiment. At extreme forward angles, the pion energies are very close to the photon energy and different kinematical cuts should lead to similar and consistent results. At larger angles, on the other hand, the shape of the NI cross section is very sensitive to the cuts made on the pion energy and small differences in the choice of the elasticity cut could lead to different results in shape and magnitude. The double differential cross section as a function of the pion polar angle $\frac{d^2\sigma}{d\theta dE_{\pi^0}}$ is directly obtained in the Monte Carlo algorithm and satisfies the normalization:

$$\int \frac{d^2\sigma}{d\theta dE_{\pi^0}} dE_{\pi^0} = 2\pi \sin\theta \left(\frac{d\sigma}{d\Omega}\right)^{\rm FSI+SHAD}. \quad (44)$$

The results for carbon and lead at 5.2 GeV and $\varepsilon_{\pi^0} \geqslant 0.92$ are presented in Figs. 13 and 14, respectively. At low polar angles ($\theta_{\pi^0} \lesssim 2°$), the pion spectra exhibit a sharp peak close to the photon energy, since the nuclear excitation is small for low-momentum transfer. The effect of the Pauli principle is also observed for lower angles, where the pion spectra decrease about one order of magnitude from 1.25 to 0.25°. At larger angles ($\theta_{\pi^0} \gtrsim 2°$) the spectra are typically shifted 50 to 100 MeV from the photon energy, with the Pb results showing longer tails at lower energies due to the larger phase space. These spectra clearly show that the elasticity cuts applied on the pion energy ($\varepsilon_{\pi^0} \gtrsim 0.9$) do not change the results of the NI cross sections, which are concentrated within higher elasticity ranges ($\varepsilon_{\pi^0} \gtrsim 0.96$).

3. *$A_{\rm eff}$ factors for π^0 photoproduction from complex nuclei: Revisiting the Cornell experiment*

The total cross section for nondiffractive meson photoproduction from complex nuclei is expected to scale with the single-nucleon cross section:

$$\sigma_{\gamma A} = A_{\rm eff}\sigma_{\gamma N}, \quad (45)$$

where $A_{\rm eff}$ represents the effective number of nucleons that contribute to the photoproduction. Consequently, we can obtain $A_{\rm eff}$ from the MCMC model results, since:

$$A_{\rm eff} = \frac{\int \left(\frac{d\sigma}{d\Omega}\right)^{\rm FSI+SHAD} d\Omega}{\int \left(\frac{d\sigma_n}{d\Omega}\right) d\Omega} = \frac{A\int \left(\frac{d\sigma}{d\Omega}\right)^{\rm FSI+SHAD} d\Omega}{\int \left(\frac{d\sigma}{d\Omega}\right)^{\rm PWIA} d\Omega}. \quad (46)$$

Previous measurements of the $A_{\rm eff}$ factors were performed at Cornell [29] for several nuclei. The π^0 yields from complex nuclei were measured in the range $0.10 < |t| < 0.25\,({\rm GeV}/c)^2$ and the $A_{\rm eff}$ factors were obtained normalizing the complex nuclei data to the deuteron data. Such procedure did not permit a model-independent measurement of $A_{\rm eff}$, since the normalization was sensitive to the Glauber corrections in the deuteron target. Despite of this limitation of Cornell's data, it is still very important to confront theory and experiment. The $A_{\rm eff}$ factors provide information about the magnitude of the cross sections from complex nuclei and the MCMC cascade model consists of an important framework for the interpretation of the data. Obviously future experiments in complex nuclei are very welcome to provide more accurate and model-independent results for $A_{\rm eff}$ and to establish more precisely the range of applicability of the nuclear models.

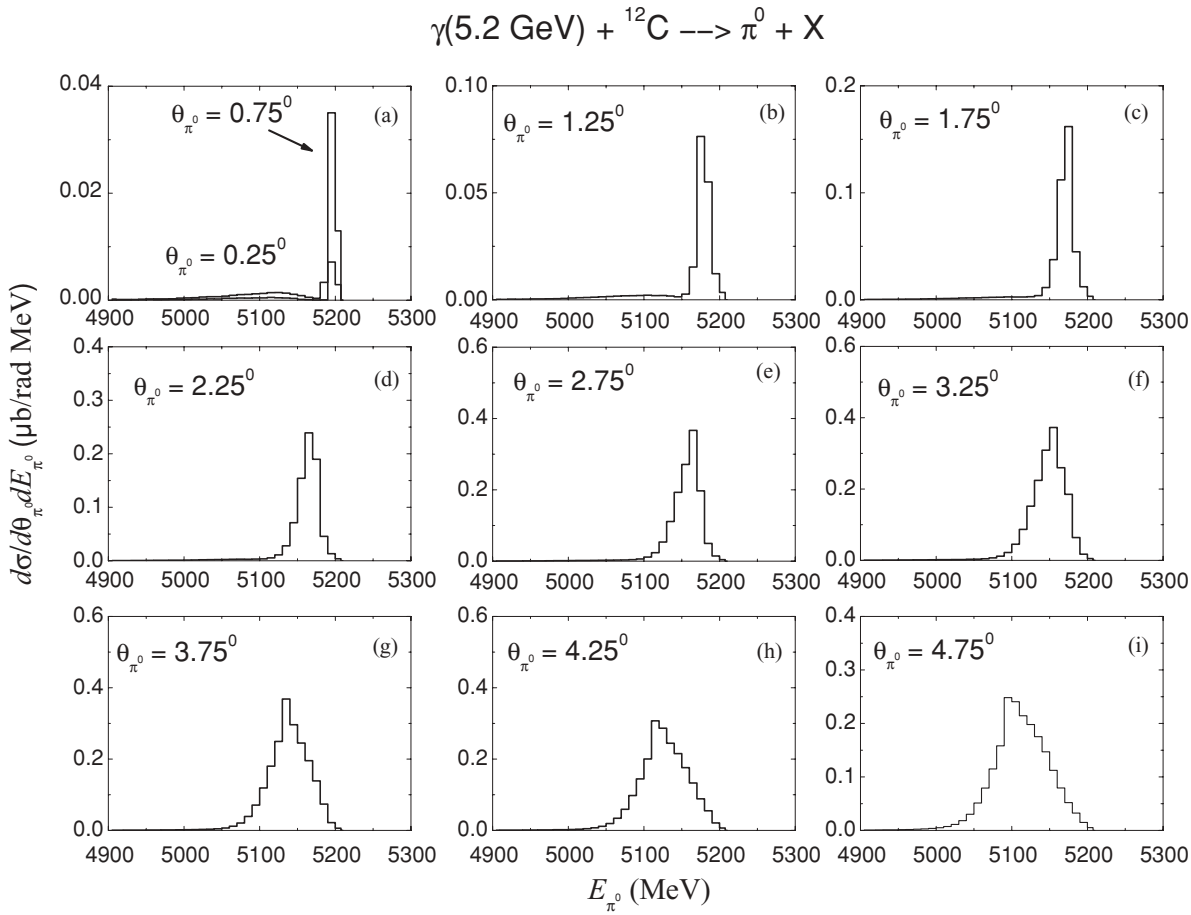

FIG. 13. Double differential cross section for incoherent π^0 photoproduction from carbon at 5.2 GeV. The histograms represent the pion spectra at selected polar angles (Lab. frame) of the photoproduced pions.

The diffractive contribution (coherent photoproduction) in Cornell's yields vanishes within the range of momentum transfer adopted in their analysis [29]. Therefore, the predictions of the cascade model for the NI cross sections are suitable for the description of the Cornell data, assuming that the Glauber corrections to the deuteron target are satisfactory [56]. Furthermore, the range of polar angles covered in their experiment ($2.3^\circ \lesssim \theta_{\pi^0} \lesssim 8.9^\circ$) and also the range of pion elasticity ($\varepsilon_{\pi^0} \gtrsim 0.87$) assures that the single π^0 photoproduction channel largely dominates the yields. The results of the $A_{\rm eff}$ factors obtained in the MCMC model are presented in Fig. 15 together with the Cornell data. The agreement between the calculations and the data is remarkable with our results reproducing both the energy (3.2 to 8.6 GeV) and target (Be to Pb) dependences of the data. Such result shows for the first time that the DESY [34] and SLAC [36] data for the elementary photoproduction cross sections are mutually consistent with the complex nuclei data from Cornell [29].

Figure 16 presents the differential cross sections ($\frac{d\sigma}{dt}$) for carbon [Fig. 16(a)] and lead [Fig. 16(b)] at $\langle E_{\pi^0}\rangle \sim$6.4 GeV. The dotted vertical lines show the range of momentum transfer integrated in Cornell's analysis. The ratio between the shaded area and the area within the dotted lines represent our values of $A_{\rm eff}$ such that:

$$A_{\rm eff} = A\frac{\int_{0.1}^{0.25}\left(\frac{d\sigma}{dt}\right)^{\rm FSI+SHAD}dt}{\int_{0.1}^{0.25}\left(\frac{d\sigma}{dt}\right)^{\rm PWIA}dt}. \tag{47}$$

Alternatively, the $A_{\rm eff}$ factors can be calculated using the integral formalism of Glauber. In this model, the following expression is deduced for high-energy pions:

$$A_{\rm eff}^{G} = \frac{2\pi}{\sigma_{\pi^0 N}}\int_0^\infty\left[1-\exp\left(-\sigma_{\pi^0 N}\int_{-\infty}^{\infty}N(b,z)\,dz\right)\right]bdb, \tag{48}$$

where $\sigma_{\pi^0 N}$ is the total $\pi^0 N$ cross section and $N(b,z)$ the nuclear density with $r^2 = b^2 + z^2$. For $\langle E_{\pi^0}\rangle \sim 6.4$ GeV, we have $\sigma_{\pi^0 N} \sim 27$ mb and Eq. (48) gives $A_{\rm eff}^{G} = 7.2$ for carbon and 60.1 for lead. The results are typically 28 and 43% higher than the MCMC results for carbon and lead, respectively. Such systematic increase in $A_{\rm eff}^{G}$ in comparison with the MCMC results is at some extent associated with the shadowing effect, which is neglected in Eq. (48). Moreover, for the case of π^0 photoproduction from carbon at 5.2 GeV [see Fig. 11(a)], we also found results 25 to 30% lower than the predictions of Ref. [4] around the peak angle ($\theta_{\pi^0} \sim 3.5^\circ$) and within the range of momentum transfer adopted in Cornell's analysis

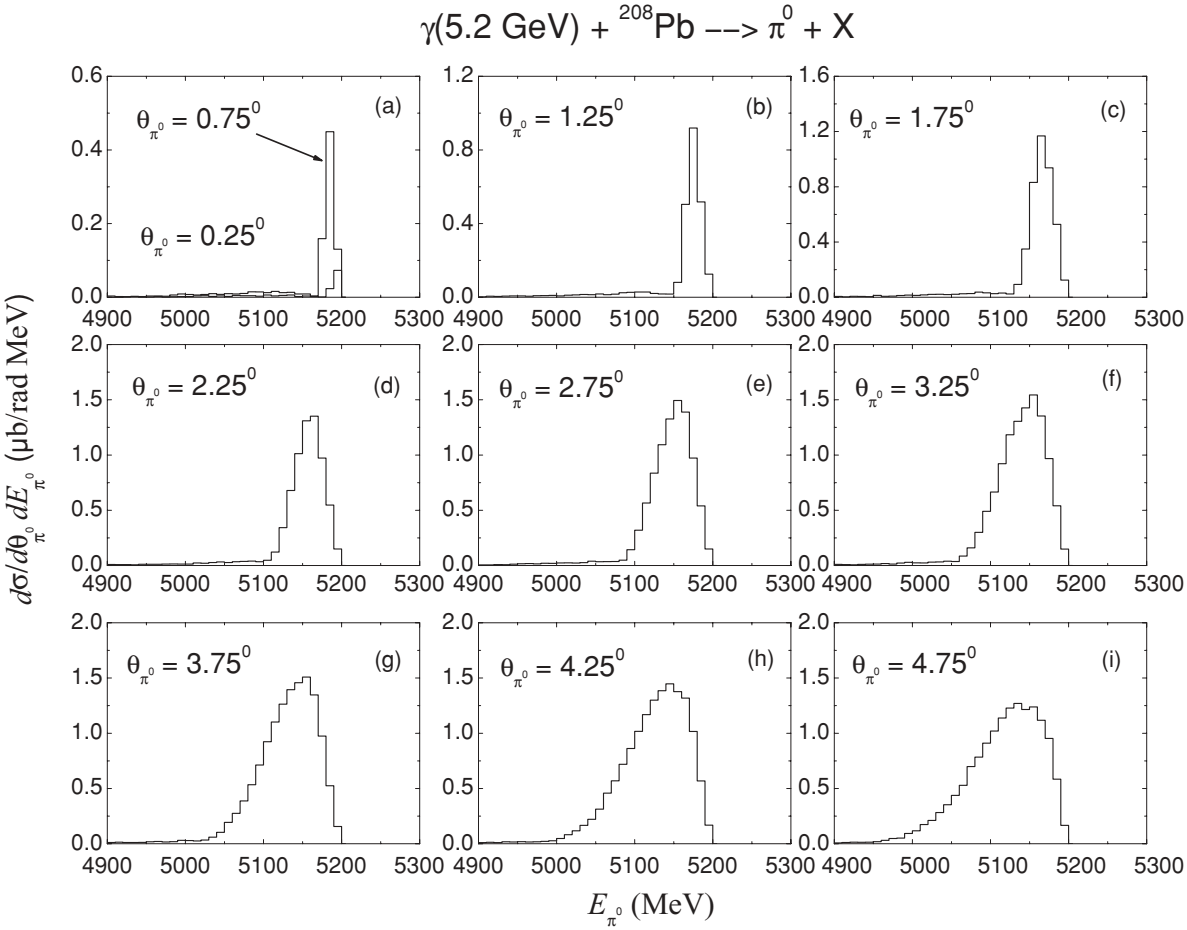

FIG. 14. Double differential cross section for incoherent π^0 photoproduction from lead at 5.2 GeV. The notation is the same as in Fig. 13.

[29]. For that reason, the magnitude of $A_{\rm eff}^{G}$ for carbon found in Eq. (48) is consistent with the reported values of Ref. [4] and approximately 25 to 30% above the MCMC results and the Cornell data (see Fig. 15).

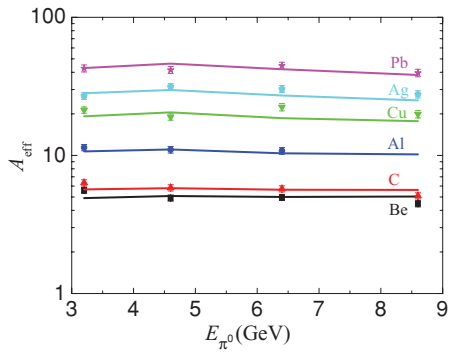

FIG. 15. (Color online) $A_{\rm eff}$ factors obtained in the MCMC model (solid lines) in comparison with Cornell data [29]. The calculations assume a pion elasticity of $\varepsilon_{\pi^0} \geqslant 0.906$ for the average energies $\langle E_{\pi^0}\rangle = 3.2$, 6.4 and 8.6 GeV and $\varepsilon_{\pi^0} \geqslant 0.870$ for $\langle E_{\pi^0}\rangle = 4.6$ GeV. The cascade results were integrated in the range $0.10 < |t| < 0.25$ (GeV/c)^2 according with Eq. (47).

Figure 17 shows the results of $\frac{(\frac{d\sigma}{dt})^{\rm FSI+SHAD}}{A_{\rm eff}}$ obtained in the MCMC model for $\langle E_{\pi^0}\rangle \sim 6.4$ GeV in comparison with the strong part of the proton cross section, which represents the cascade input. As easily observed, the results for light nuclei (Be and C) exhibit a sharp peak around $|t| \sim 0.1$ GeV^2, following the general trend of the nucleon cross section. For the case of intermediate and heavy nuclei, on the other hand, the collisional broadening due to a more effective Fermi motion and a stronger meson-nucleus FSI attenuates the structure at 0.1 GeV^2. The results found for complex nuclei obviously satisfy the condition $\frac{1}{A_{\rm eff}}\int(\frac{d\sigma}{dt})^{\rm FSI+SHAD}dt = \int \frac{d\sigma_n}{dt}dt$, as expected from Eq. (45). Such result indicates that the accurate MD adopted for light nuclei is crucial for the delineation of the t dependence of the cross sections.

B. η photoproduction

1. *Single differential cross sections for incoherent η photoproduction from complex nuclei*

The calculations for incoherent η photoproduction followed the same steps adopted for π^0 photoproduction, except for the evaluation of the FSI. As previously explained, the η-nucleon interaction is not well understood and the total and elastic η-nucleon cross sections are unknown. On the other hand,

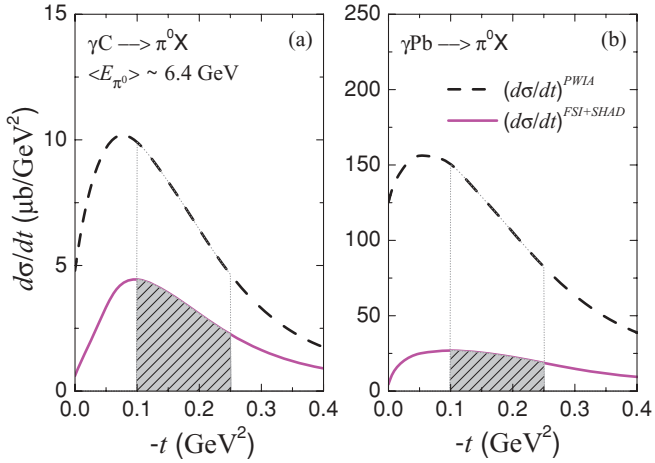

FIG. 16. (Color online) Differential cross sections ($\frac{d\sigma}{dt}$) for incoherent π^0 photoproduction from (a) carbon and (b) lead at $\langle E_{\pi^0}\rangle \sim 6.4$ GeV. The dashed black lines represent the PWIA, while the solid magenta lines are the final results from the cascade model. The vertical dotted lines show the range of momentum transfer adopted in Cornell experiment.

the η-nucleon cross section is expected to be smaller than the π^0-nucleon cross section due to the strangeness content of the η meson. Furthermore, the magnitude of the total η-nucleon cross section could be estimated combining the data from complex nuclei with the MCMC model calculations. Unfortunately, these data are not available in absolute scale and for the calculations that followed we have assumed $\sigma_{\eta N\to\text{Total}} = C\,\sigma_{\pi^0 N\to\text{Total}}$ and $\frac{\sigma_{\eta N\to\eta N}}{\sigma_{\eta N\to\text{Total}}} = \frac{\sigma_{\pi^0 N\to\pi^0 N}}{\sigma_{\pi^0 N\to\text{Total}}}$. The scaling factor C was varied between 0.5 and 1 in order to verify its influence on the NI cross sections. Fortunately, the relevant results and conclusions that will be presented in this section are not sensitive to the scaling factor C, they depend only on the final shape of the cross sections.

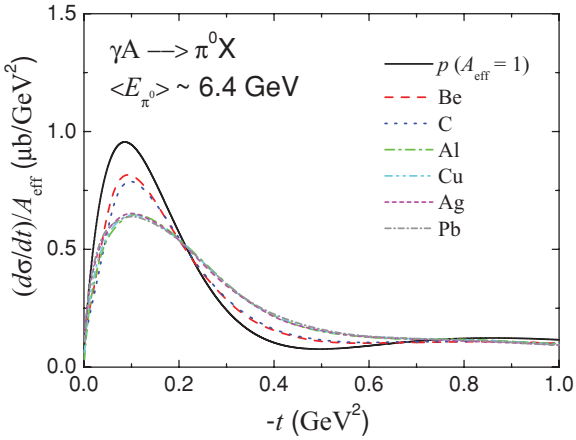

FIG. 17. (Color online) Differential cross sections $\frac{(\frac{d\sigma}{dt})}{A_{\text{eff}}}$ for incoherent π^0 photoproduction from Be (dashed red), C (dotted blue), Al (dashed-dotted green), Cu (dashed double dotted cyan), Ag (short dashed magenta), and Pb (short dashed-dotted gray) obtained in the MCMC model. The solid black line represents the strong part of the elementary photoproduction cross section [Eq. (8)].

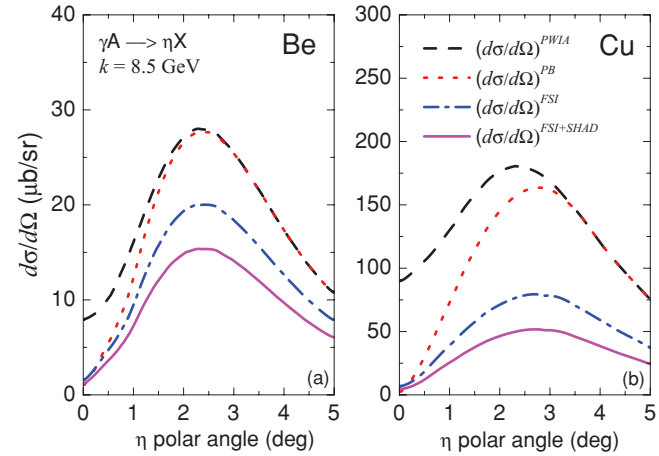

FIG. 18. (Color online) Differential cross section for incoherent η photoproduction from (a) Be and (b) Cu at 8.5 GeV. The notation is the same as in Fig. 11, where we have assumed $\varepsilon_\eta \geqslant 0.89$.

The MCMC results for incoherent η photoproduction from Be and Cu at 8.5 GeV are presented in Fig. 18, where we have used $C = 1$ and an elasticity cut of 0.89 on the total meson energy. The notation is the same adopted for π^0 photoproduction (Fig. 11).

The influence of the scaling factor C on the NI cross section was investigated running the cascade model with a smaller η-nucleon cross section. The results for incoherent η photoproduction from Be at $k = 8.5$ GeV [$\frac{d\sigma}{d\theta} = 2\pi \sin\theta (\frac{d\sigma}{d\Omega})^{\text{FSI+SHAD}}$] and $\varepsilon_\eta \geqslant 0.89$ are presented in the left panel of Fig. 19 for $C = 0.5$ (dashed black line), $C = 0.75$ (dotted red line), and $C = 1$ (solid blue line). The right plot of Fig. 19 shows the respective ratios of the cross sections to the result obtained with $C = 1$. Above typically 1°, a 25% reduction of the η-nucleon cross section ($C = 0.75$) leads to a 7.5% increase in the NI cross section. A further 25% reduction of the η-nucleon cross section ($C = 0.5$) also increases the NI cross section

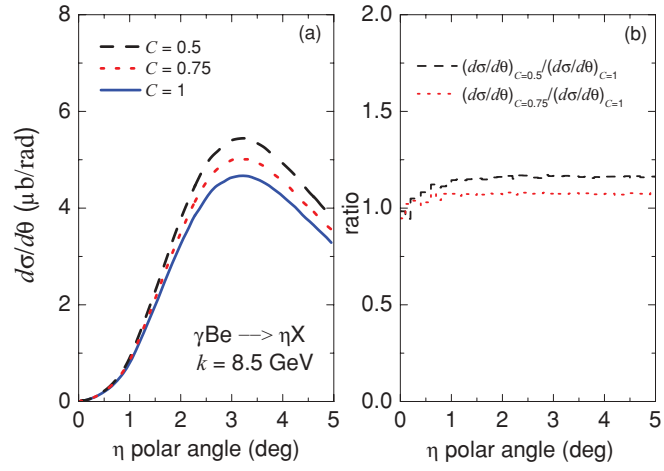

FIG. 19. (Color online) (a) Differential cross section ($\frac{d\sigma}{d\theta}$) for incoherent η photoproduction from Be assuming $C = 0.5$ (dashed black line), $C = 0.75$ (dotted red line), and $C = 1$ (solid blue line). (b) Cross section ratios between the results for $C = 0.5$ (dashed black) and $C = 0.75$ (dotted red) and the reference result for $C = 1$.

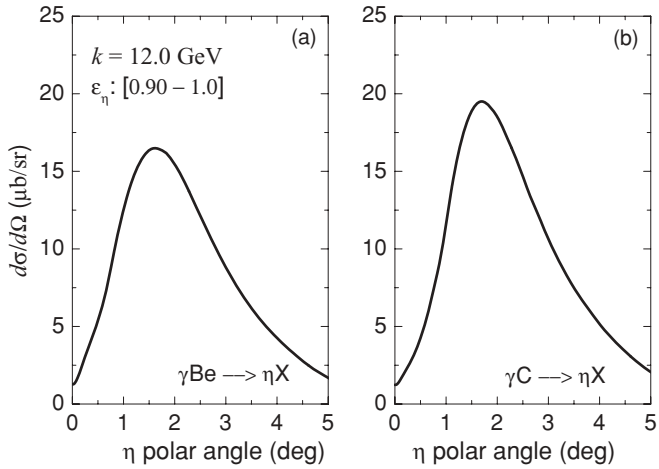

FIG. 20. Differential cross section for incoherent η photoproduction from (a) Be and (b) C at 12.0 GeV. The solid black lines are the final results from the cascade model assuming an elasticity cut of 0.90 on the meson energy.

by approximately the same amount ($\sim$16%). Below 1°, the results for $C = 0.5$ and $C = 0.75$ are typically within 10% of the reference result for $C = 1$. The cascade model results at 12 GeV are shown in Figs. 20(a) for Be and 20(b) C, where we have used $C = 1$ and $\varepsilon_\eta \geqslant 0.9$.

In order to compare the shapes of the NI cross sections for π^0 and η photoproduction, we have scaled our final results obtained for η by the ratio of the corresponding elementary photoproduction cross sections at 12 GeV and $t \simeq -0.1$ GeV^2: $(d\sigma_n/dt)^{\pi^0}_{t=-0.1} \approx 5(d\sigma_n/dt)^{\eta}_{t=-0.1}$. The results are shown in Figs. 21(a) for Be and 21(b) C, where one easily observes that the cross sections exhibit quite different shapes. The η photoproduction cross section peaks at higher angles than the π^0 cross section, which falls more abruptly at larger angles. Such difference in shape is related with the t dependence of the elementary photoproduction cross sections, where a dip around

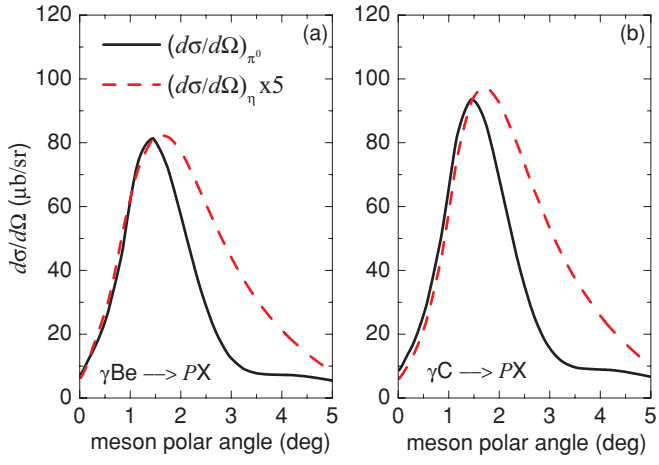

FIG. 21. (Color online) Differential cross sections for incoherent π^0 (solid black lines) and η (dashed red lines) photoproduction from (a) Be and (b) C at 12.0 GeV. The results for η photoproduction are multiplied by a factor 5, which is approximately the ratio between the elementary photoproduction cross sections at $|t| \sim 0.1$ (GeV/c)^2.

$|t| \approx 0.5$ (GeV/c)^2 is clearly evident for π^0 photoproduction (see Figs. 1 and 2).

2. *Extracting the $\eta \to \gamma\gamma$ decay width via the Primakoff method: Revisiting the Cornell experiment*

At extreme forward angles, the total cross section for pseudoscalar meson photoproduction from complex nuclei is assumed to be in the form [2,3,23,57,58]:

$$\frac{d\sigma}{d\Omega} = |T_P + e^{i\varphi} T_{\rm NC}|^2 + |T_{\rm NI}|^2, \tag{49}$$

where T_P, $T_{\rm NC}$, and $T_{\rm NI}$ represent the relevant amplitudes for the photoproduction mechanism. The amplitudes T_P and $T_{\rm NC}$ are related with coherent meson photoproduction via the exchange of a virtual photon (T_P) or a vector meson ($T_{\rm NC}$). The interference phase-angle φ between these two amplitudes plays an essential role at forward angles and is usually treated as a free parameter. The remaining amplitude $T_{\rm NI}$ is related with incoherent photoproduction.

As deduced by H. Primakoff, the Coulomb amplitude is the sum of the amplitudes from the protons such that [1]:

$$T_P = [8\alpha Z^2 \Gamma_{P\to\gamma\gamma}]^{\frac{1}{2}} \left(\frac{\beta}{\mu}\right)^{\frac{3}{2}} \frac{k^2}{Q^2} \widetilde{F}_C(k,\theta) \sin\theta, \tag{50}$$

where $\alpha \simeq 1/137$, Z is the atomic number, and $Q^2 = -t$ is the four-momentum transfer. $\widetilde{F}_C(k,\theta)$ represents the electromagnetic form factor (FF) including meson-nucleus FSI, while β and θ are the velocity and production angle (Lab. frame) of the photoproduced meson, respectively.

The nuclear coherent (NC) amplitude is given by:

$$T_{\rm NC} = A \widetilde{F}_{\rm NC}(k,\theta) L \sin\theta, \tag{51}$$

where $\widetilde{F}_{\rm NC}(k,\theta)$ is the strong FF taking into account FSI and $L \sin\theta$ is the spin-nonflip nucleon amplitude. Such amplitude is not known precisely at our energies of interest and we adopted the same parametrization of Ref. [23] for the case of η photoproduction ($L = 4k$).

The NI cross section is obtained from the cascade calculations such that:

$$|T_{\rm NI}|^2 = \left(\frac{d\sigma}{d\Omega}\right)^{\rm FSI+SHAD}. \tag{52}$$

Consequently, the shape of the total cross section $\frac{d\sigma}{d\Omega}$ is dependent on the radiative decay width $\Gamma_{P\to\gamma\gamma}$ and on the interference phase angle φ, which are usually free parameters to be obtained via a fitting to the complex nuclei data. Furthermore, the magnitudes of the NC and NI contributions are also generally left free to account for the inaccuracies in the absolute value of the spin-nonflip amplitude $L \sin\theta$ and also to account for the compatibility between the complex nuclei data and the proton data, which provide the normalization of the NI cross section (see Figs. 1 and 2).

For the case of Cornell experiment [23], on the other hand, the cross sections of η photoproduction from complex nuclei were not published and the only information available are the meson yields, which are the number of two γ events within the invariant mass of the η meson at a given angular

bin. Therefore, in order to compare theory and experiment, a separate Monte Carlo algorithm was developed to account for the $\eta \to \gamma\gamma$ decay. This routine collects the number of η events according with the MCMC results for the double differential cross sections $\frac{d^2\sigma}{d\theta dE_\eta}$ that simultaneously satisfy the selection criteria from Cornell experiment regarding the geometry acceptance and kinematical cuts. With this routine, we were able to write the number of η events at a given angular bin $n(\theta)$ in terms of *shape factors* for the three components of the cross section:

$$n(\theta) = a_P S_P(\theta) + a_{\rm NC} S_{\rm NC}(\theta) + a_{\rm NI} S_{\rm NI}(\theta) + 2\sqrt{a_P a_{\rm NC}} \cos\varphi \sqrt{S_P(\theta) S_{\rm NC}(\theta)}, \quad (53)$$

where S_P, $S_{\rm NC}$, and $S_{\rm NI}$ [59] are, respectively, the shapes for the Coulomb, NC, and NI contributions; with a_P, $a_{\rm NC}$, $a_{\rm NI}$, and φ constants to be determined by fitting the complex nuclei data from Cornell [23].

Our reanalysis of Cornell's decay width proposes the interpretation of the η photoproduction yields from Be and Cu at $E_b = 9$ GeV. The U data, on the other hand, are not included since the Primakoff and NC contributions peak almost in the same angles without an adequate angular resolution in Cornell experiment to disentangle these terms unambiguously. This FF issue was discussed in N. A. Roe (p. 1451) [60] and will be addressed later.

The shapes for the Coulomb and NC components of Eq. (53) were taken from Cornell's analysis [23] to assure that the only difference between Cornell's and this approach is the inelastic part (NI). Such contribution was assumed to be isotropic, energy independent, and proportional to $A^{\frac{3}{4}}$ in Cornell's analysis ($T_b = 1.0A^{0.75}\mu$b/sr) and is more deeply investigated in this work. Furthermore, Cornell's shapes include angular resolution effects, which are very relevant specially for S_P due to its typical sharp peak at forward angles.

The shapes of $S_{\rm NI}(\theta)$ for Be and Cu were then calculated neglecting angular resolution effects and folding the two γ events from the MC routine with a flat bremsstrahlung spectrum. The shapes for the two γ events as a function of photon energy and meson polar angle $S_{\rm NI}(k,\theta)$ were calculated from 8 to 9 GeV in 100-MeV steps. This procedure was employed considering that only the mesons with high elasticity $\varepsilon_\eta \gtrsim 0.89$ ($8.05 \lesssim E_\eta \lesssim 9.0$ GeV) could satisfy the maximum $\gamma\gamma$ opening angle cut of 0.137 rad adopted in Cornell's analysis for $E_b = 9$ GeV [23]. Figure 22 presents our results of $S_{\rm NI}(k,\theta)$ for Be in relative scale (left plot) taken at three different incident energies. The right plot shows our final result for Be after folding $S_{\rm NI}(k,\theta)$ with the bremsstrahlung spectrum.

In order to verify our method to obtain the shapes of $S_{\rm NI}(\theta)$ that satisfy Cornell's geometry and kinematics, we have also calculated with the same algorithm the expected two γ events from η decay due to incoherent photoproduction assuming isotropic distribution $S_{\rm NI}^{\rm ISOT}(\theta)$ and neglecting the Pauli blocking. The result of this simulation is presented by the histogram of Fig. 23 and reproduces quite reasonably the shape obtained in Cornell's analysis (solid red line), which also assumes isotropic distribution without Pauli blocking. Consequently, the shapes of $S_{\rm NI}(\theta)$ that were obtained for Be and Cu effectively account for the detection geometry and kinematical cuts applied in Cornell's analysis.

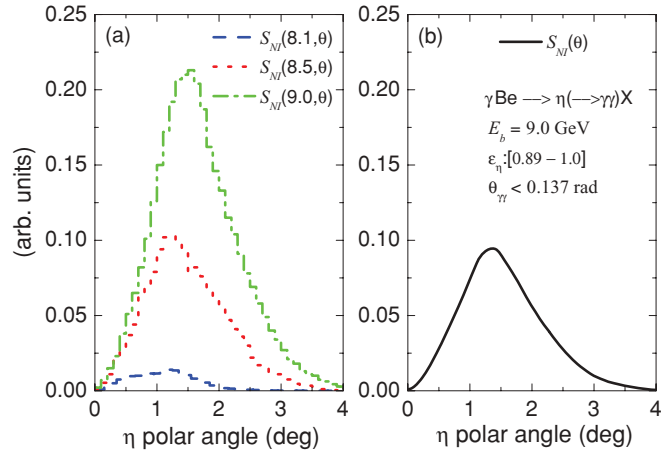

FIG. 22. (Color online) *Shape factors* in relative scale for the two γ decay events due to incoherent η photoproduction from Be, including Cornell's detection geometry and kinematical cuts [23]. (a) NI *shape factors* for $k = 8.1$ GeV (dashed blue), $k = 8.5$ GeV (dotted red), and $k = 9.0$ GeV (dashed-dotted green) as a function of the meson polar angle. (b) NI *shape factor* after folding the cascade results within 8 to 9 GeV with a flat bremsstrahlung spectrum. The calculations consider Cornell's geometry, meson elasticity regime ($\varepsilon_\eta \geqslant 0.89$), and maximum γ-γ opening angle cut ($\theta_{\gamma\gamma} \leqslant 0.137$ rad).

The P and NC components of Eq. (53) are generally strongly correlated due to the contribution of the interference term. On the other hand, the NC cross section scales with A^2 [Eq. (51)] and one should expect that a single parameter, namely $a_{\rm NC}$, should fit simultaneously the complex nuclei data from Be and Cu. However, the magnitude of the NC cross section is also sensitive to FSI, which are in principle included in the FF calculations. Furthermore, the interference

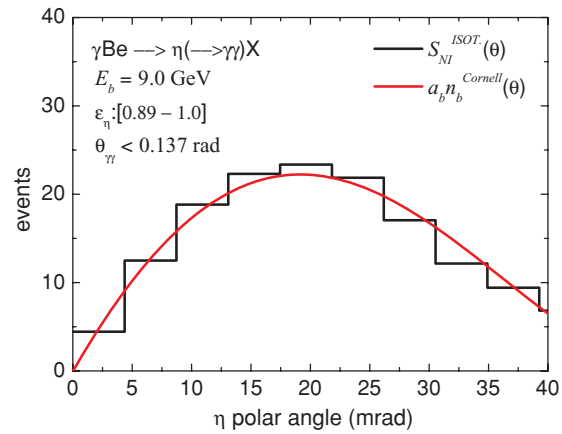

FIG. 23. (Color online) MCMC calculations (solid black histogram) for the two γ events from η decay assuming isotropic NI photoproduction without Pauli blocking and including Cornell's geometry and kinematical cuts. The red solid line is the NI background obtained in Cornell's analysis also neglecting Pauli blocking and assuming isotropic photoproduction ($T_b = 1.0A^{0.75}\mu$b/sr). The MCMC calculations are normalized such that $\int S_{\rm NI}^{\rm ISOT}(\theta)\,d\theta = \int a_b n_b^{\rm Cornell}(\theta)\,d\theta$.

TABLE III. Fitting results of Cornell's data from Be and Cu at $E_b = 9$ GeV. The first line represents our best χ^2 result for a seven parameter fitting combining Be and Cu results. Lines two, three, and four present illustrative fits for fixed phase shifts. The last line shows the results fitting Be data only. Details in the text.

	a_P(keV)	$a_{\rm NC}$	$\frac{a_b \int n_b^{\rm Cornell}(\theta) d\theta}{a_{\rm NI} \int S_{\rm NI}(\theta) d\theta}$	φ(rad)	$\frac{\chi^2}{\rm DOF}$
Be	0.476(62)	0.89(32)	0.957(70)	0.59(52)	$\frac{71.09}{70}$
Cu		6.3(13)	1.10(13)	1.88(19)	
Be	0.341(29)	1.07(15)	1.006(67)	0.0 (fixed)	$\frac{96.26}{72}$
Cu		0.93(27)	0.950(90)		
Be	0.470(26)	1.92(20)	1.079(83)	$\frac{\pi}{2}$ (fixed)	$\frac{112.93}{72}$
Cu		3.41(56)	1.03(11)		
Be	0.381(27)	1.42(17)	1.045(74)	1.0 (fixed)	$\frac{100.06}{72}$
Cu		1.54(38)	0.971(97)		
Be only	0.512(90)	0.97(46)	0.964(72)	0.83(43)	$\frac{36.08}{35}$

phase angle φ is also sensitive to FSI and should be different for different targets. The fitting parameter $a_{\rm NC}$ is strongly correlated with the interference phase angle and is also affected by the correlation between S_P and $S_{\rm NC}$. Obviously these correlations differ for Be and Cu and it is not recommended to impose a single NC parameter to fit both data sets simultaneously.

So by inserting the shapes of S_P, $S_{\rm NC}$, and $S_{\rm NI}$ in Eq. (53), we were able to refit simultaneously Be and Cu data from Cornell using a 7-parameter fitting (a_P, $a_{\rm NC}^{\rm Be}$, $a_{\rm NC}^{\rm Cu}$, $a_{\rm NI}^{\rm Be}$, $a_{\rm NI}^{\rm Cu}$, $\varphi^{\rm Be}$, and $\varphi^{\rm Cu}$). The best χ^2 results are presented in the first line of Table III. The parameters a_P and $a_{\rm NC}$ were obtained using the ratios between the Primakoff and NC events found in our fitting and found in Cornell's analysis with the respective fitting parameters for the same data set (second line of Table I from Ref. [23]). The contribution of the NI term is presented in the third column, where we show the ratio (always consistent with unit) between the NI events found in Cornell's analysis $[\int a_b n_b^{\rm Cornell}(\theta)\, d\theta]$ and in our calculations $[\int a_{\rm NI} S_{\rm NI}(\theta)\, d\theta]$. Additional fits for fixed phase shifts were also performed to illustrate the strong correlations between $a_P/a_{\rm NC}$ and φ. For instance, the $a_{\rm NC}$ parameters for Cu vary by a factor of 4 considering constructive ($\varphi = 0$) and no interference ($\varphi = \frac{\pi}{2}$). This complicated scenario is attributed to the big overlap between S_P and $S_{\rm NC}$ for intermediate and heavy nuclei due to a FF effect, without adequate angular resolution from Cornell experiment. For instance, at $k \sim 8.5$ GeV, the Primakoff peak (target independent to first order) is $\sim$3.5 mrad, while the NC peak angle is $\sim$19, 10, and 7 mrad for Be, Cu, and U, respectively. So, the Primakoff and NC peak angles for intermediate and heavy nuclei are typically 5 mrad apart. The angular bin in Cornell's data was taken as 1 mrad, making it difficult to establish one unambiguous fitting of the Primakoff and NC components for Cu and Pb. In fact, the Cornell group found five different NC parameters in their analysis (fourth column of Table I from Ref. [23]). For instance, for a machine energy of 5.8 GeV (Be, Cu, and U) and 11.45 GeV (U only) they found $a_N = 0.25 \pm 0.24$ and $a_N = 0.24 \pm 0.60$, respectively. These numbers are consistent with zero and a factor of 4 to 5 lower than the results found in the other fits, reflecting the strong correlations previously mentioned. These strong correlations provide clear evidences for the discrepancy in the value of $\Gamma_{\eta\to\gamma\gamma}$ obtained at Cornell after averaging the results from Be, Al, Cu, Hg, and U; making salient the advantage of using light nuclei for similar measurements within this kinematics. To stress our hypothesis, we have also performed a fitting to the Be data only (last line of Table III). As easily verified, the fitted parameters found in this analysis are consistent with our main results for Be. The interference phase angle ($\varphi^{\rm Be} = 0.83 \pm 0.43$ rad) is also consistent with the result expected from the Regge theory (neglecting FSI): $\varphi_{\rm Regge} \simeq \tan^{-1}[\frac{{\rm Im}F_1(t=0)}{{\rm Re}F_1(t=0)}] = \frac{\pi[1-\alpha(0)]}{2} = 0.958$ rad.

Figure 24 shows our main results for Be and Cu in comparison with Cornell's data (upper plots). At extreme forward angles, the Primakoff (dotted blue lines) and the interference (short-dashed cyan lines) terms largely dominate the yields. At higher angles, the NC (dashed-dotted green lines) and NI (dashed-double-dotted magenta lines) contributions become the most relevant processes. We have also found a significant interplay between the P, NC, and INT terms for Cu, where a destructive interference is observed (see discussion below). The cascade results for the NI components are essential to fit the data at larger angles, where the other terms simply vanish. The lower plots of Fig. 24 present a comparison between the NI backgrounds from MCMC calculations (solid black lines) and Cornell's isotropic approach (dashed red lines) obtained for Be and Cu. As verified, Cornell's NI backgrounds both for Be and Cu are approximately four times higher than the MCMC predictions under the Primakoff peak ($\sim$3.5 mrad), since they have assumed an isotropic NI cross section. The MCMC background, on the other hand, is strongly suppressed at forward angles due to the exclusion principle. Despite of this difference in shape, the number of NI events from the MCMC calculations and from Cornell are consistent with each other even for the illustrative fits for fixed phase shifts (third column of Table III). Our final reported values of the decay width correspond to our main result obtained for Be and Cu $\Gamma_{\eta\to\gamma\gamma} = 0.476(62)$ keV and also to the single fitting of Be data $\Gamma_{\eta\to\gamma\gamma} = 0.512(90)$ keV. The errors of the decay widths include only the statistical errors from the fits and should be interpreted as lower limits of our analysis.

There are two main sources of uncertainties on the extracted decay width related with the evaluation of the nuclear effects of Pauli blocking in light nuclei and η-nucleus FSI. The systematic uncertainty due to the Pauli blocking depends strictly on the γ-nucleon kinematics, Fermi momentum, and meson-scattering angle (Fig. 2). The γ-nucleon kinematics depends essentially on the momentum distribution of the struck nucleon, while the other two sources are safely constrained by the experimental data and introduce negligible effects on the decay width. The uncertainty due to the momentum distribution was estimated by fitting Cornell's data with the MCMC output that provided the most significant difference from our reference value obtained with the PWIA of Ref. [42] (Fig. 24). This output was obtained using the empirical distribution from a NIKHEF experiment [61] (see Fig. 2 from Ref. [45]), leading to a systematic uncertainty in the decay

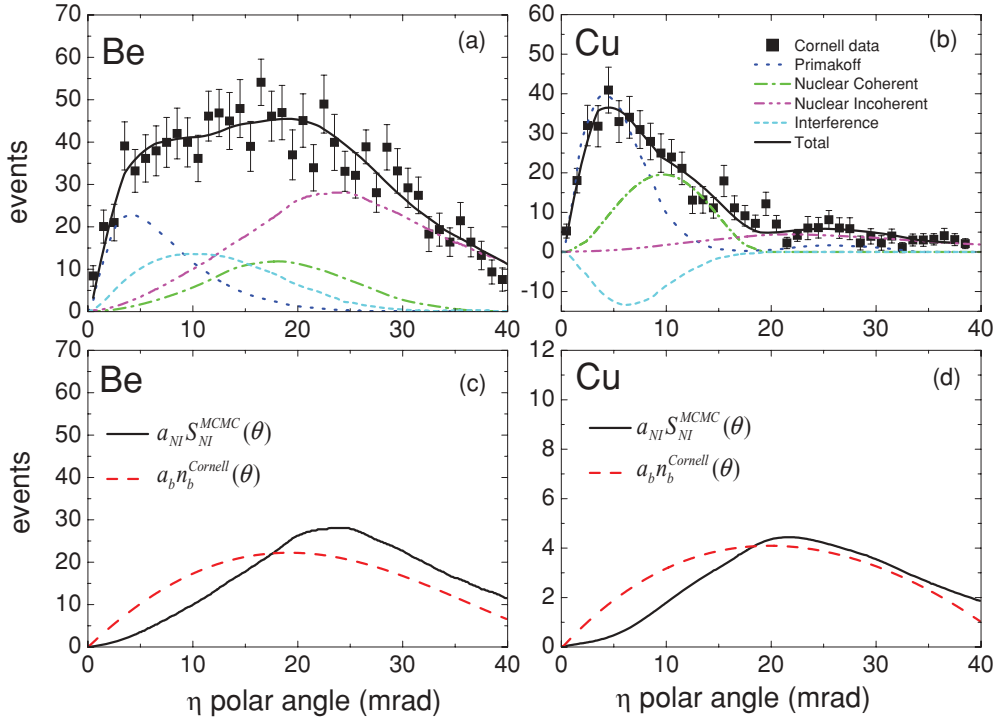

FIG. 24. (Color online) (Upper panels) η photoproduction yields from (a) Be and (b) Cu at $E_b = 9$ GeV (data points) and fitted *shape factors* of the Primakoff (dotted blue), NC (dashed-dotted green), NI (dashed-double-dotted magenta), and interference (short-dashed cyan) components of the total yield (solid black). The data points and the shapes of S_P and $S_{\rm NC}$ were taken from Ref. [23]. (Lower panels) Fitted NI contributions from the MCMC model $a_{\rm NI}S_{\rm NI}(\theta)$ (solid black) and from Cornell $a_b n_b^{\rm Cornell}(\theta)$ (dashed red) for (c) Be and (d) Cu.

width of less than 2% for the combined fit (Be and Cu) and less than 4% for the single fit (Be only).

The uncertainty in the decay width due to the η nucleus FSI was estimated assuming a robust variation (50%) in the η-nucleon cross section. Since this variation introduces an almost isotropic effect, the corresponding systematic error is vanishing small both for the simultaneous (<0.2%) and single (<0.1%) fits.

So, the uncertainty in the decay width due to the model error can be safely estimated to be less than 4%. Such value is much lower than the statistical uncertainties for the combined (13%) and single (17.6%) fits and one order of magnitude lower than the discrepancy between Cornell and collider measurements (∼50%).

Figure 25(a) presents some of the experimental results for the $\eta \to \gamma\gamma$ decay width obtained in collider experiments [17–20] (squares) and via the Primakoff method at Cornell [23] (circle). The PDG average of 0.510(26) keV [25] is shown by the solid red line. The right plot shows our results (triangles) from the reanalysis of Cornell's yields from Be and Cu and Be only in comparison with collider measurements. Despite of our limitations related with the experimental systematic uncertainties (see discussion below), our results are in sharp contrast (∼50–60%) with the value obtained at Cornell and in nice agreement with the collider measurements.

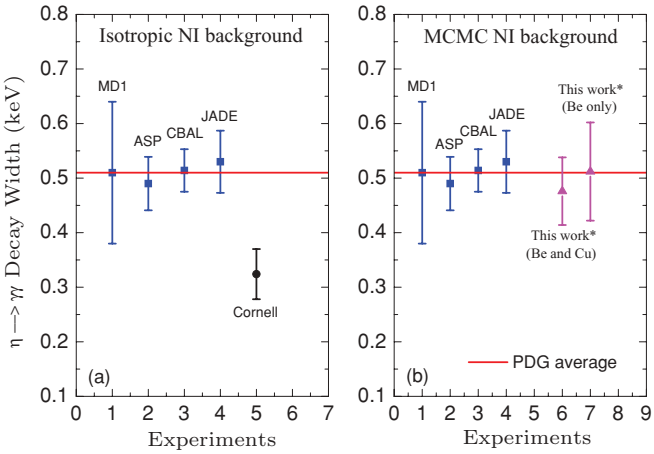

FIG. 25. (Color online) (a) $\eta \to \gamma\gamma$ decay width measurements obtained in collider experiments (squares) [17–20] that participate to the PDG average (solid red line) of 0.510(26) keV [25] and via the Primakoff method at Cornell [23] (circle). (b) Comparison between collider measurements [17–20] (squares) and the results obtained in our reanalyses (triangles). The asterisk indicates that the errors of the decay widths are purely statistical.

V. CONCLUSIONS AND FINAL REMARKS

A sophisticated calculation based on an extended version of the MCMC intranuclear cascade model was proposed to study incoherent photoproduction of pseudoscalar mesons (π^0 and η) from complex nuclei. The calculations coupled for the first time an accurate description of the elementary photoproduction mechanism (Sec. I) with important nuclear

effects in high-energy photon-nucleus interaction (Sec. III). The results for π^0 and η photoproduction were concentrated at forward angles within 4 to 12 GeV and covered a large range of target masses (Be to Pb).

The calculations for π^0 photoproduction reproduced with good accuracy the magnitude and energy dependence of the measured ratios $\sigma_{\gamma A}/\sigma_{\gamma N}$ from Cornell [29]. This result also shows for the first time that the proton data from DESY [34] and SLAC [36] are consistent with the complex nuclei data from Cornell. It is worth mentioning, however, that the Cornell data were sensitive to the Glauber corrections to the deuteron and additional cross section measurements with tagged photon beams are strongly encouraged for the verification of the MCMC cascade model.

Our reanalysis of Cornell's η photoproduction yields propitiated the extraction of the $\eta \to \gamma\gamma$ decay width by a simultaneous fitting of Be and Cu data at $E_b = 9$ GeV [$\Gamma_{\eta\to\gamma\gamma} = 0.476(62)$ keV] and also using Be data only [$\Gamma_{\eta\to\gamma\gamma} = 0.512(90)$ keV]. These results are in sharp contrast ($\sim$50–60%) with the value reported by the Cornell group [0.324(46) keV] and in line with the PDG average, as shown by the right plot of Fig. 25. The systematic uncertanty on the extracted decay width due to our model error is estimated to be less than 4%.

The inelastic background of η mesons in Cornell experiment [23] was attributed to the NI photoproduction mechanism. Such procedure was the same adopted in Cornell's analysis, where they fitted the data using four components of the cross section [Eq. (53)]. The main difference between this and Cornell's analysis is the parametrization of the NI cross section. This NI term was calculated for the first time for η photoproduction within 8 to 9 GeV using the MCMC model and represents a significant improvement in comparison with the unphysical isotropic term used by the Cornell group. In fact, this isotropic term without Pauli blocking was also used by the Cornell group for the extraction of the $\pi^0 \to \gamma\gamma$ decay width [57]. Fortunately, for the case of π^0 photoproduction, the Primakoff peak angle is approximately 16 times lower than for η photoproduction ($\frac{m^2_{\pi^0}}{m^2_{\eta}} \simeq \frac{1}{16}$), making the decay width much less sensitive to the parametrization of the NI term (few percentages level). This argument represents a plausible explanation for the huge discrepancy ($\sim$60%) in the $\eta \to \gamma\gamma$ decay width obtained via the Primakoff effect in Cornell in comparison with collider measurements, since the NI term plays an important role within the Primakoff peak.

Additionally with the better description of the NI background, our analysis also differs from Cornell's with respect to the data that was fitted. In Cornell, data from light, intermediate and heavy nuclei were fitted simultaneously to extract the decay width. In our approach, however, we have restricted the analysis to Be and Cu data only. As easily verified in Fig. 2 from Ref. [23], the Primakoff, NC, and interference terms for U peak almost at the same angles. This poor experimental scenario generates a dramatic correlation between the fitted parameters due to the strong overlap between the P and NC components of the cross sections. For instance, Cornell group obtained a_N parameters (Table I from Ref. [23]) consistent with zero for the fits at 5.8 GeV (Be, Cu, and U) and 11.45 GeV (U only). For that reason, the averaging procedure adopted in Cornell's analysis is strong evidence for the discrepancy in the decay width, since they have mixed strongly correlated fitted parameters. These strong correlations also appeared in our reanalysis of the Cu data, where a destructive P-NC interference provided the best fit. Such destructive interference has absolutely no relationship with the NI term, which reproduced the data at larger angles with good accuracy. It is most likely related with the poor experimental scenario in Cornell's data for Cu and should be further verified in a more precise high-resolution experiment before any conclusive statement.

There are some important restrictions in our reanalysis of Cornell's data [23] that should be carefully mentioned: (a) The effect of the angular resolution was neglected when folding $S_{\rm NI}(k,\theta)$ with the bremsstrahlung spectrum, (b) the bremsstrahlung spectrum was assumed to be flat within 8 to 9 GeV, (c) U data were discarded in the analysis, and (d) the experimental systematic uncertainties were neglected in the reported errors of the decay widths. Approximations (a) and (b) were verified at some extent when we recovered Cornell's background term assuming isotropic photoproduction (Fig. 23). Approximation (c) was necessary due to the strong correlations for U previously mentioned, while approximation (d) reflects our inability to recover all necessary information to claim for a superceded decay width measurement. In fact, our goal was to deliver a consistent explanation of the discrepancy in Cornell's $\eta \to \gamma\gamma$ decay width based on a sophisticated calculation of the NI background, without the necessary accuracy to supercede Cornell's measurement though.

In conclusion, additional cross section measurements of π^0 and η photoproduction from the proton and from complex nuclei are strongly recommended with the advent of the 12-GeV upgrade of the Jefferson Laboratory. These measurements, together with the state-of-the-art cascade calculations for the NI term, would propitiate the extraction of more precise values for the radiative decay widths of pseudoscalar mesons via the Primakoff method. The elementary photoproduction cross sections are the necessary inputs for the cascade calculations and new measurements both for π^0 and η photoproduction at extreme forward angles are desirable to fix more accurately the parameters of the Regge models. The nuclear measurements, in our understanding, should be concentrated in light systems, such as Be and C, due to the combination of a sizable Primakoff contribution ($\sim Z^2$) and a smaller correlation between the Coulomb and nuclear coherent terms in comparison with intermediate and heavy nuclei. The He target is also interesting and complementary to light nuclei, but one should expect stronger correlations between the NC and NI terms due to a FF effect. The measurements should encompass larger angles to fix more accurately the NI cross section, which also constraints the magnitude of the NC component. With the NC magnitude more accurately determined, the phase shift and decay width are also better determined.

ACKNOWLEDGMENTS

We wish to thank the PrimEx Collaboration for the motivation of some of the improvements of the MCMC

model. We are also indebted to Professor A. M. Bernstein for various illuminating discussions and to Professor O. Helene for reviewing our statistical considerations. We also thank the Brazilian agency FAPESP for the partial support to this work.

[1] H. Primakoff, Phys. Rev. **81**, 899 (1951).
[2] G. Faldt, Nucl. Phys. **43**, 591 (1972).
[3] C. A. Engelbrecht, Phys. Rev. **133**, B988 (1964).
[4] S. Gevorkyan, A. Gasparian, L. Gan, I. Larin, and M. Khandaker, arXiv:0908.1297v1 [hep-ph].
[5] B. Krusche *et al.*, Eur. Phys. J. A **22**, 277 (2004).
[6] C. M. Tarbert *et al.*, Phys. Rev. Lett. **100**, 132301 (2008).
[7] C. Bennhold and H. Tanabe, Nucl. Phys. A **530**, 625 (1991); M. Hedayati-Poor and H. S. Sherif, *ibid.* **740**, 309 (2004); Phys. Rev. C **76**, 055207 (2007).
[8] R. C. Carrasco, Phys. Rev. C **48**, 2333 (1993); R. C. Carrasco, E. Oset, and L. L. Salcedo, Nucl. Phys. A **541**, 585 (1992).
[9] T. Yorita *et al.*, Phys. Lett. B **476**, 226 (2000); H. Yamazaki *et al.*, Nucl. Phys. A **670**, 202 (2000); T. Kinoshita *et al.*, Phys. Lett. B **639**, 429 (2006).
[10] J. Lehr, M. Post, and U. Mosel, Phys. Rev. C **68**, 044601 (2003); J. Lehr, M. Effenberger, and U. Mosel, Nucl. Phys. A **671**, 503 (2000).
[11] [http://www.jlab.org/primex/primex_notes/PR99-014.ps] (PrimEx Proposal).
[12] J. L. Goity, A. M. Bernstein, and B. R. Holstein, Phys. Rev. D **66**, 076014 (2002).
[13] B. Ananthanarayan and B. Moussallam, J. High Energy Phys. 05 (2002) 052.
[14] K. Kampf and B. Moussallam, Phys. Rev. D **79**, 076005 (2009).
[15] J. S. Bell and R. Jackiw, Nuovo Cimento A **60**, 47 (1969); S. L. Adler, Phys. Rev. **177**, 2426 (1969).
[16] B. L. Ioffe and A. G. Oganesian, Phys. Lett. B **647**, 389 (2007).
[17] S. E. Baru *et al.*, Z. Phys. C **48**, 581 (1990).
[18] N. A. Roe *et al.*, Phys. Rev. D **41**, 17 (1990).
[19] D. A. Williams *et al.*, Phys. Rev. D **38**, 1365 (1988).
[20] W. Bartel *et al.*, Phys. Lett. B **160**, 421 (1985).
[21] H. Aihara *et al.*, Phys. Rev. D **33**, 844 (1986).
[22] A. J. Weinstein *et al.*, Phys. Rev. D **28**, 2896 (1983).
[23] A. Browman, J. DeWire, B. Gittelman, K. M. Hanson, E. Loh, and R. Lewis, Phys. Rev. Lett. **32**, 1067 (1974).
[24] C. Bemporad, P. L. Braccini, L. Foà, K. Lübelsmeyer, and D. Schmitz, Phys. Lett. B **25**, 380 (1967).
[25] K. Nakamura *et al.* (Particle Data Group), J. Phys. G **37**, 075021 (2010).
[26] T. E. Rodrigues, J. D. T. Arruda Neto, J. Mesa, C. Garcia, K. Shtejer, D. Dale, I. Nakagawa, and P. L. Cole, Phys. Rev. Lett. **101**, 012301 (2008).
[27] T. E. Rodrigues, J. D. T. Arruda Neto, J. Mesa, C. Garcia, K. Shtejer, D. Dale, and I. Nakagawa, Phys. Rev. C **71**, 051603(R) (2005).
[28] T. E. Rodrigues, J. D. T. Arruda Neto, J. Mesa, C. Garcia, K. Shtejer, D. Dale, and I. Nakagawa, Braz. J. Phys. **36**, 1366 (2006).
[29] W. T. Meyer, A. Browman, K. Hanson, A. Osborne, A. Silverman, and F. E. Taylor, Phys. Rev. Lett. **28**, 1344 (1972).
[30] J. S. Ball, Phys. Rev. **124**, 2014 (1961).
[31] G. F. Chew, M. L. Goldberger, F. E. Low, and Y. Nambu, Phys. Rev. **106**, 1345 (1957).
[32] A. Gasparian and S. Gevorkyan (private communication).
[33] J. S. Ball, W. R. Frazer, and M. Jacob, Phys. Rev. Lett. **20**, 518 (1968).
[34] M. Braunschweig, W. Braunschweig, D. Husmann, K. Lübelsmeyer, and D. Schmitz, Nucl. Phys. B **20**, 191 (1970).
[35] W. Braunschweig, W. Erlewein, H. Frese, K. Lübelsmeyer, H. Meyer-Wachsmuth, D. Schmitz, A. Schultz von Dratzig, and G. Wessels, Phys. Lett. B **33**, 236 (1970).
[36] R. L. Anderson, D. B. Gustavson, J. R. Johnson, I. D. Overman, D. M. Ritson, B. H. Wiik, and D. Worcester, Phys. Rev. D **4**, 1937 (1971).
[37] R. Anderson, D. Gustavson, J. Johnson, D. Ritson, B. H. Wiik, W. G. Jones, D. Kreinick, F. Murphy, and R. Weinstein, Phys. Rev. D **1**, 27 (1970).
[38] J. Dewire, B. Gittelman, R. Loe, E. C. Loh, D. J. Ritchie, and R. A. Lewis, Phys. Lett. B **37**, 326 (1971).
[39] A. Sibirtsev, J. Haidenbauer, S. Krewald, U.-G. Meißner, and A. W. Thomas, Eur. Phys. J. A **41**, 71 (2009).
[40] A. Sibirtsev, J. Haidenbauer, S. Krewald, and U.-G. Meißner, Eur. Phys. J. A **44**, 169 (2010).
[41] T. E. Rodrigues, J. D. T. Arruda Neto, D. Dale, and P. Cole, in *Proccedings of the VIII Latin American Symposium on Nuclear Physics and Applications*, *Santiago, 2009* (to be published).
[42] L. Lapikas, G. van der Steenhoven, L. Frankfurt, M. Strikman, and M. Zhalov, Phys. Rev. C **61**, 064325 (2000).
[43] T. de Forest Jr., Nucl. Phys. A **392**, 232 (1983).
[44] E. J. Moniz, I. Sick, R. R. Whitney, J. R. Ficenec, R. D. Kephart, and W. P. Trower, Phys. Rev. Lett. **26**, 445 (1971).
[45] T. E. Rodrigues, J. D. T. Arruda Neto, J. Mesa, C. Garcia, K. Shtejer, D. Dale, I. Nakagawa, and P. Cole, in *Proccedings of the VII Latin American Symposium on Nuclear Physics and Applications, Cuzco, 2007* (AIP, Melville, NY, 2007), Vol. 947, p. 101.
[46] T. H. Bauer, R. D. Spital, and D. R. Yennie, Rev. Mod. Phys. **50**, 261 (1978).
[47] Aachen-Berlin-Bonn-Hamburg-Heidelberg-München Collaboration, Phys. Lett. B **27**, 474 (1968).
[48] J. Ballam *et al.*, Phys. Rev. Lett. **21**, 1544 (1968).
[49] T. E. Rodrigues, J. D. T. Arruda Neto, A. Deppman, V. P. Likhachev, J. Mesa, C. Garcia, K. Shtejer, G. Silva, S. B. Duarte, and O. A. P. Tavares, Phys. Rev. C **69**, 064611 (2004).
[50] J. Cugnon, T. Mizutani, and J. Vandermeulen, Nucl. Phys. A **352**, 505 (1981); J. Cugnon, *ibid.* **462**, 751 (1987); J. Cugnon, C. Volant, and S. Vuillier, *ibid.* **620**, 475 (1997); A. Boudard, J. Cugnon, S. Leray, and C. Volant, Phys. Rev. C **66**, 044615 (2002); S. Leray *et al.*, *ibid.* **65**, 044621 (2002); J. Benlliure *et al.*, Nucl. Phys. A **700**, 469 (2002); J. Cugnon and P. Henrotte, Eur. Phys. J. A **16**, 393 (2003).
[51] J. R. Cudell, V. V. Ezhela, P. Gauron, K. Kang, Yu. V. Kuyanov, S. B. Lugovsky, B. Nicolescu, and N. P. Tkachenko, Phys. Rev. D **65**, 074024 (2002).
[52] Robert J. Cence, *Pion-Nucleon Scattering* (Princeton University Press, Princeton, NJ, 1969), p. 61.

[53] M. L. Perl, L. W. Jones, and C. C. Ting, Phys. Rev. **132**, 1252 (1963).
[54] K. J. Foley, S. J. Lindenbaum, W. A. Love, S. Ozaki, J. J. Russell, and L. C. L. Yuan, Phys. Rev. Lett. **11**, 425 (1963).
[55] K. J. Foley, R. S. Jones, S. J. Lindenbaum, W. A. Love, S. Ozaki, E. D. Platner, C. A. Quarles, and E. H. Willen, Phys. Rev. **181**, 1775 (1969).
[56] The range of momentum transfer in Cornell experiment ($0.10 < |t| < 0.25$ (GeV/c)^2) guarantees that the diffractive processes (nuclear coherent and electromagnetic) do not contribute in the yields. However, the contribution of the decay products of vector mesons (ρ and ω) is very relevant within this kinematics, but they were clearly separated in the Cornell experiment [29].
[57] A. Browman, J. DeWire, B. Gittelman, K. M. Hanson, D. Larson, E. Loh, and R. Lewis, Phys. Rev. Lett. **33**, 1400 (1974).
[58] G. Morpurgo, Nuovo Cimento **31**, 569 (1964).
[59] A different notation is employed in Ref. [23] for the Primakoff ($a_C n_C$), NC ($a_N n_N$), and NI ($a_b n_b$) components of Eq. (53).
[60] L. Montanet *et al.* (Particle Data Group), Phys. Rev. D **50**, 1173 (1994).
[61] G. van der Steenhoven, H. P. Blok, E. Jans, M. De Jong, L. Lapikás, E. N. M. Quint, and P. K. A. De Witt Huberts, Nucl. Phys. A **480**, 547 (1988).